Master of Science Thesis

Inlet Distortion Characterization of the Boundary Layer Ingesting D8 Aircraft

NASA N+3 Project

Elise van Dam

March 10, 2015

Faculty of Aerospace Engineering

Delft University of Technology

Inlet Distortion Characterization of the Boundary Layer Ingesting D8 Aircraft

NASA N+3 Project

Master of Science Thesis

For obtaining the degree of Master of Science in Aerospace
Engineering at Delft University of Technology

Elise van Dam

March 10, 2015

Faculty of Aerospace Engineering · Delft University of Technology

Delft University of Technology **Massachusetts Institute of Technology**

DELFT UNIVERSITY OF TECHNOLOGY
DEPARTMENT OF AERODYNAMICS

The undersigned hereby certify that they have read and recommend to the Faculty of Aerospace Engineering for acceptance the thesis entitled **"Inlet Distortion Characterization of the Boundary Layer Ingesting D8 Aircraft"** by **Elise van Dam** in fulfillment of the requirements for the degree of **Master of Science**.

Dated: March 10, 2015

Supervisors:

Prof.Dr.ir. G. Eitelberg

Dr. A.G. Rao

Prof.Dr.ir. L.L.M. Veldhuis

Dr. M.D. Pavel

Abstract

This thesis experimentally assesses the inflow towards the propulsors and the pressure distribution at the propulsor fan-face for the boundary layer ingesting D8 aircraft, and examines the dependence of the model, the propulsor and the flight condition on the inlet distortion. Use is made of mini-tuft flow visualization and five hole probe pressure surveys. The results are compared with CFD simulations. The experiments were performed at the most important mission points of the D8: cruise, descent, start of climb, and top of climb. CFD was only performed for cruise and top of climb. From the pressure distributions the distortion coefficient, DC(60), was calculated, the maximum variation in pressure over a specified circumferential segment (60°).

At cruise the DC(60) equaled ~ 0.3, compared to DC(60)$\sim$ 0.1-0.2 for conventional aircraft. The D8 model caused cross-flow to the propulsors, the flow is directed towards the sides of the model. Both fans rotate in the same direction, such that one propulsor has the flow in the direction of rotation, and the other has the flow opposite to the direction of rotation, causing an asymmetry between the left and right propulsor. The flight phase is characterized by α, the angle of attack, λ, the ratio of tip velocity over tunnel speed, and β, the yaw angle. It is found that at a high value of λ the pressure differences at the fan-face are reduced by engine suction, lowering the distortion and counter-acting the cross-flow. A low value of λ means a relative lower influence of the propulsor on the flow, such that the propulsor is not able to (fully) counter-act the cross-flow, resulting in a higher difference in DC(60) and power required between the left and right propulsor. Changing α mainly changes the location of the pressure distributions.

The results from experiments agree well with CFD, there is a 1% deviation in DC(60) at top of climb condition, and 6% at cruise. The pressure distributions look similar and the pressure coefficient values scale equally, from -0.8 to 0.

Further research should focus on the exact fan response on the distortion. The D8 used conventional engines, optimized for uniform inflow. Developing a BLI optimized engine could further increase the BLI benefit. The D8 model induced cross-flow, resulting in an asymmetry between the left and right engine. Eliminating this cross-flow by a change in model design could also decrease the distortion.

Acknowledgments

This work is supported by the NASA's Fundamental Aeronautics program, the Fixed Wing project, through Cooperative Agreement Number NNX11AB35A. The author is part of a larger team, and the work would not have been possible without the help of the N+3 team, consisting of NASA, Aurora Flight Sciences, Pratt&Whitney and MIT.

I would first like to thank my thesis supervisor at the MIT, Edward Greitzer. For giving me the chance to come to MIT to work on the N+3 project and for being a great supervisor. I am honored that I was part of this team and I could not have learned more this year. You gave me the freedom to pick up my own projects, but made me think first about the reason why it was important, what I would learn from it, and what I would need (and from who) to do it.

I would like to thank my supervisors at the TU Delft, Georg Eitelberg and Arvind Rao, for approving and supporting my decision to perform my Master's thesis at MIT, and for keeping me focused on graduating while being part of a larger project group.

I am grateful to the MIT N+3 team, consisting of Neil Titchener, Nina Siu, Michael Lieu, Cécile Casses, David Hall, Arthur Huang, Alejandra Uranga, Mark Drela and Edward Greitzer. In particular for the great teamwork during six week test campaign at NASA Langley.

I thank the 14x22 foot Subsonic Wind tunnel staff at NASA Langley for their help with the wind tunnel experiments, in particular Gregory Gatlin and test engineer Jim Byrd. And I thank Shishir Pandya from NASA Ames for the execution of the CFD calculations.

I would like to thank my office mates, Devon Jedamski and George Christou for being such awesome office mates. Thank you for the interesting discussions, random chats, but above all for your humor.

Last of all, I would like to acknowledge the grants I received to make this year possible, Stichting dr. Hendrik Muller's Vaderlandsch Fonds, College van Bestuur fonds, Universiteitsfonds Delft, KIVI Studie- en Reisfonds and the Van der Maas fonds.

Table of Contents

List of Figures

List of Tables

Chapter 1

Introduction

The International Air Transport Association (IATA) reported an average annual growth rate in passenger demand of 6.3% over the past ten years and IATA also expects a 31% rise in passenger demand between 2012 and 2017 (IATA). A major issue accompanying this growth is that more air transportation means a potential for increased environmental pollution, because of the use of petroleum-based fuel, and increased noise pollution. As a result there is more focus than ever on making aircraft more fuel efficient and quieter.

The D8 aircraft, displayed in Figure 1.1, has the potential of lowering the fuel burn by 71%, while generating 76% less emissions, and lowering the noise by 60 EPNdB (Effective Perceived noise), compared to a Boeing 737-800. This aircraft is currently being investigated by a team of MIT, Aurora Flight Sciences, Pratt&Whitney, as part of the NASA N+3 project (the term N+3 refers to three generations beyond the current aircraft flying: 2035). A main factor contributing to the fuel saving is boundary layer ingestion (BLI). BLI is estimated to result in a 15% reduction in the power required for cruise flight of which 8% comes from direct aerodynamic effects (Uranga et al. (2014)).

BLI is not a new concept and the idea dates back to 1946, when Smith and Roberts (1946) documented ways to use the boundary layer for aircraft propulsion. It has not been used in civil aircraft, because there are a number of challenges yet to be met. BLI requires an integrated configuration, to ingest the boundary layer in the propulsors, which has to be designed. The boundary layer has a non-uniform velocity and the inflow is dependent on the shape of the fuselage and the flight condition, the inlet pressure will change continuously during flight.

The main goal of this thesis is to determine *the dependence of the distortion on the D8 airframe at various points in the flight envelop*, and *to establish differences in the dis-*

Figure 1.1: D8 aircraft, picture credit: George Homich/NASA

tortion level between a BLI and a non-BLI configuration. These data are then used to *validate CFD for the BLI D8 configuration.* Once the distortion to the fan is established the fan aerodynamic and aeromechanic response can be established.

Experiments and computations have been performed to determine the inlet distortions of the D8 aircraft for the most important mission points, cruise, descent, start of climb, and top of climb. A yaw case has also been investigated. Mini-tuft flow visualization have been performed upstream of the propulsors and on the propulsor nacelles to visualize the flow entering the propulsors. Five hole probe surveys were conducted as close as possible to the propulsor fan-face to determine the inlet pressure distributions. These experimental results are compared to CFD calculations. Overflow code is used and the propulsors are modeled using an actuator disc model. From these calculations streamlines are generated and the pressure distribution at the plane of the five hole probe is calculated. The distortion coefficient DC(60) is calculated from CFD and experiments and compared to values from literature.

The thesis content is as follows, an explanation of the N+3 project and the D8 aircraft is given in Chapter 2, after which the BLI theory and benefit are given in Chapter 3. Chapter 4 gives the methodologies, and Chapter 5 describes the set-up of the experiments and computational model. Chapter 6 presents the results of the experiments and computation, which are further discussed in the conclusion, Chapter 7. Recommendations for future work are given in Chapter 8.

Chapter 2

D8 “Double Bubble” Aircraft

The D8 aircraft has been developed as part of the NASA N+3 program. This chapter gives a summary of the NASA N+3 program, and the D8 aircraft.

2.1 NASA N+3 Project

NASA set goals to drastically lower the fuel burn, noise and emissions for a new generation of aircraft (N+3), as part of the Subsonic Fixed Wing (SFW) project, where N specifies the current generation and 3 the number of generations beyond the current, which is expected to be 2035. The goals set by NASA in 2009 at the project start were (Ashcraft et al. (2011)):

1. 71 dB cumulative (sum of lateral, flyover, and approach noise certification points) reduction in aircraft noise below the FAA Stage 4 noise regulation (Federal Aviation Administration)
2. 75% reduction in landing/takeoff NOx (LTO NOx) emissions with respect to CAEP 6 (International Civil Aviation Organization)
3. 70% reduction in mission fuel burn relative to a state of the art reference aircraft
4. Investigation into new methods to more effectively utilize existing aviation infrastructure, by reducing the takeoff and landing distance required of large aircraft such that smaller, regional airports can be used.

NASA selected four subsonic teams led by The Boeing Company, GE Aviation, Lockheed Martin Corporation, Massachusetts Institute of Technology (MIT) and Northrop

Grumman to receive separate study contracts (NASA (b)) to identify key technology development needs, as well as breakthroughs to enable reaching these goals.

2.2 D8 “Double Bubble”

A result of the collaboration of MIT with Aurora Flight Sciences, Pratt&Whitney and NASA was the design of the D8 aircraft, often called the “Double Bubble” aircraft due to the shape of the aircraft, a double fuselage, which is illustrated on the left of Figure 2.4. The D8 aircraft falls in the category of the Boeing 737-800 and Airbus A320 aircraft: it is designed for 180 passengers, 3000 nm (5560 km) range transport.

The D8 was designed by Professor Mark Drela, who used Transport Aircraft System OPTimization (TASOPT) software (Drela) to get weight, aerodynamic and engine performance predictions, MSES viscous 2D airfoil code for the wing airfoil, AVL vortex-lattics code for the basic configuration lay-out and QUADPAN panel code to confirm the AVL calculations (Drela (2011)). Benefits of the D8 configuration include (Drela (2011)):

1. Smaller and lighter wings, because the fuselage generates large part of the lift, Figure 2.1
2. Reduced tail size, due to a nose-up moment caused by lift at the nose
3. Lighter landing gear support structure, due to shorter landing gear load path, Figure 2.2
4. Reduced floor-beam weight via center floor support, Figure 2.2
5. Partial span loading, due to a wider fuselage (5.5 meter versus 3.9 meter)
6. Cruise Mach number 0.72, enabling a lower sweep wing, reduced structural load and increased C_L
7. Reduced drag, due to higher aspect ratio, from use of an unswept wing
8. No leading edge slat, from increased $C_{L_{\max}}$ due to unswept wing
9. Twin-fin “Π-tail’, lightening the horizontal tail, such that minimal nacelles are needed and the fans are shielded, reducing noise. The placement of the engines enables the use of boundary layer ingestion (BLI), Chapter 3
10. Smaller horizontal tail, with two point support reducing bending moment and weight, Figure 2.2
11. Fewer windows, because the cabin is shorter.
12. Smaller vertical tail, due to smaller engines-out yaw moment
13. Faster unload/load of passengers due to a double cabin, resulting in shorter travel time, despite the lower speed (D8 flies at Mach 0.72, the B737-800 at Mach 0.8)

Figure 2.3 shows the morphing sequence of the Boeing 737-800 to the D8.6. The D8.2 represents the D8 aircraft using technology that is currently available. The D8.2 has a 40% fuel burn saving, compared to a B737-800, of which 15% is due to BLI. The D8.6 is latest version of the D8, and takes into account the technologies that are expected to be available in 2035, resulting in a 70% fuel burn saving. A comparison of the D8 and the B737-800 is given in Figure 2.4. Assumed technologies for 2035 are:

- Advanced structural materials (D8.6 is from composites, D8.1 from aluminum)
- Natural laminar flow on wing bottom
- Reduced secondary structure weight
- Active load alleviation
- Health and usage monitoring
- Advanced engine materials
- Variable area nozzle
- High Tt4 Materials and advanced cooling
- Distortion tolerant fan
- LDI (lean direct injection) advanced combustor

During Phase 1 of the project (2008-2010) the MIT team developed the D8 aircraft concept. During phase two the design was assessed through experiments and computations. Computations were performed at NASA Ames and experiments were performed in two entries in the NASA Langley 14x22 foot Subsonic Wind tunnel (entry 1: August 2013, entry 2: August & September 2014).

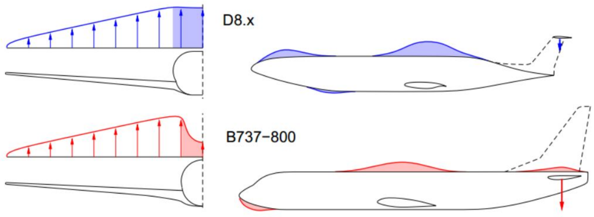

Figure 2.1: Increased fuselage lift and built-in nose-up moment from nose lift, Drela (2010)

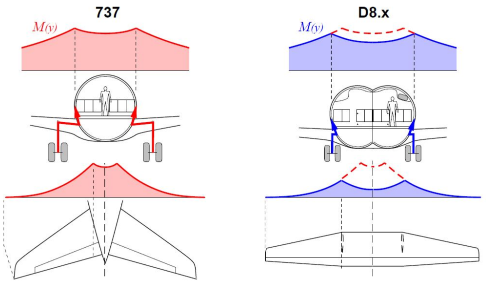

Figure 2.2: Fuselage reduces wing and tail bending moments, and shortens landing gear load paths, Drela (2011)

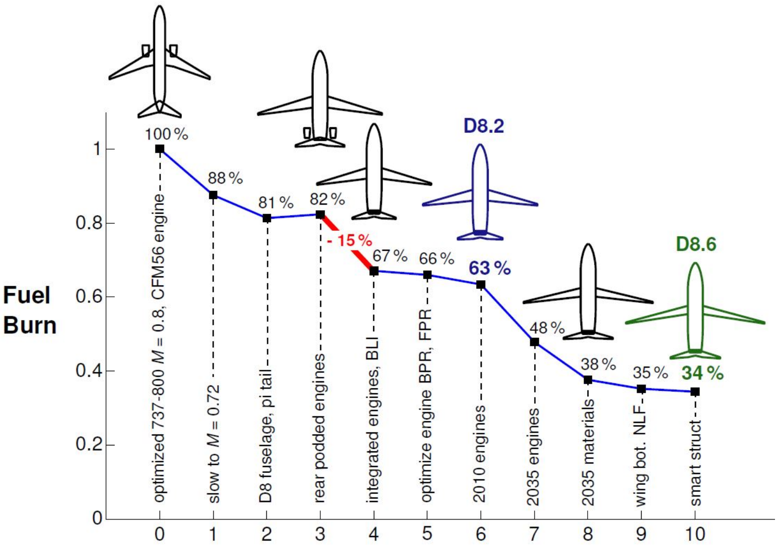

Figure 2.3: Morphing Sequence: B737-800 → D8.6, Drela et al. (2015)

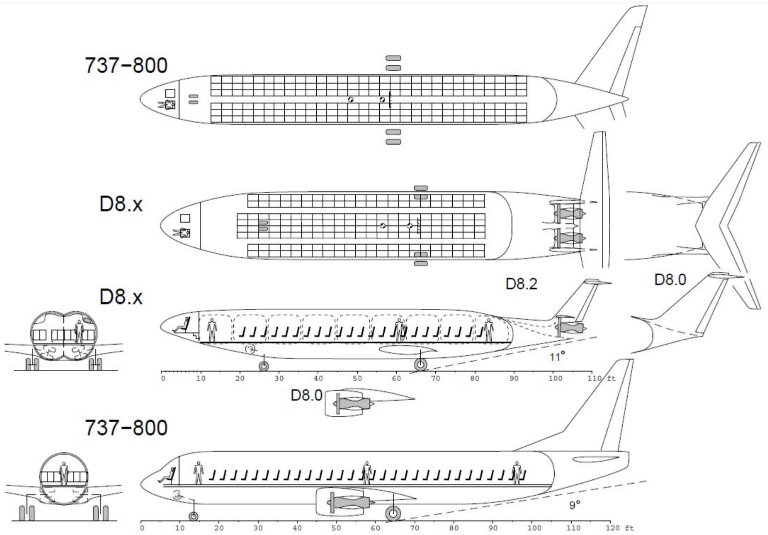

Figure 2.4: D8 and B737-800, side and top-view comparison, Drela (2011)

Chapter 3

Boundary Layer Ingestion (BLI)

This section discusses the theory and advantages of BLI, the method of assessing the BLI benefit and the challenges for BLI configuration.

3.1 BLI Principle

Boundary layer ingestion (BLI) literally means ingesting the boundary layer from the fuselage and/or wing (depending on the placement of the configuration) into the propulsion system.

The BLI advantage is a combination of aerodynamic and system-level benefits, and dependent on the configuration used.

3.1.1 BLI Aerodynamics

Plas (2006) compared a BLI configuration with a podded configuration (a configuration with podded engines, i.e. engines embedded in nacelles mounted on pylons). For the podded configuration, the engines accelerate the free stream inflow at u_∞, to a velocity u_j, creating a momentum excess, which balances the momentum deficit due to the drag of the airframe, as in Figure 3.1. The force the engine needs to provide is equal to the mass flow, times the increase in velocity. For the BLI configuration the inflow is not the free stream flow u_∞, but the velocity of the aircraft wake, u_w. The force provided by the engine is thus

$$F_{\text{engine, no BLI}} = \dot{m}(u_j - u_\infty) = \dot{m}(u_\infty - u_w)_{\text{ideal case}} = D_{\text{airframe}} \tag{3.1}$$

$$F_{\text{engine, BLI}} = \dot{m}(u_j - u_w) = \dot{m}(u_\infty - u_w)_{\text{ideal case}} = D_{\text{airframe}}. \tag{3.2}$$

If, as assumed by Plas (2006), the drag of the airframe, D_{airframe}, is not affected by BLI, both the podded and the BLI configuration need to overcome the same drag. It is however expected that an integrated BLI configuration will experience more drag than a podded configuration, making this a very rough assumption.

The rate of mechanical energy, P, added to the flow, is equal to the difference in kinetic energy between inflow and outflow

$$P_{\text{added, no BLI}} = \frac{\dot{m}}{2}(u_j^2 - u_\infty^2) = \frac{F}{2}(u_j + u_\infty) \tag{3.3}$$

$$P_{\text{added, BLI}} = \frac{\dot{m}}{2}(u_j^2 - u_w^2) = \frac{\dot{m}}{2}(u_\infty^2 - u_w^2) = \frac{F}{2}(u_w + u_\infty). \tag{3.4}$$

Because u_w is lower than u_j, the added power to propel the same body is lower using BLI. In other words, for the same force, less power needs to be added to the flow.

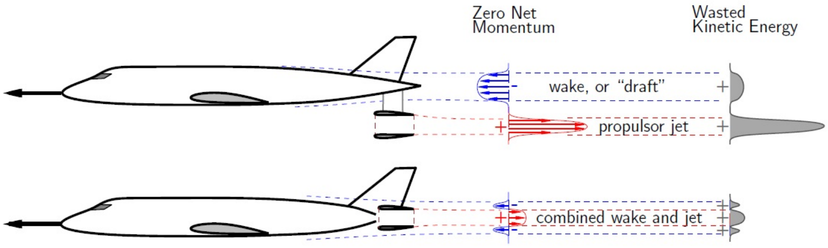

Figure 3.1: Benefits of BLI: podded case and 100% BLI, MIT et al. (2014)

Another way to explain the aerodynamic BLI benefit is to use the power balance method, developed by Drela (2009), in which he evaluates the mechanical power and kinetic energy of the flow. He derives a mechanical power balance equation, given as Equation 3.5, in terms of the mechanical power supply and the dissipation.

$$P_K = \Phi \tag{3.5}$$

For a control volume, which completely surrounds the propulsor as in Figure 3.2, Equation 3.5 states that the net mechanical power, P_K is equal to the dissipation, Φ. The latter consists of the jet dissipation, Φ_{jet}, wake dissipation, Φ_{wake}, fuselage dissipation, Φ_{fuselage}, and vortex dissipation, Φ_{vortex}. The power balance becomes:

$$P_K = \Phi_{\text{fuselage}} + \Phi_{\text{jet}} + \Phi_{\text{wake}} + \Phi_{\text{vortex}} \tag{3.6}$$

For incompressible flow, P_K is equal to the volume flux of total pressure, the difference in total pressure between the flow at the inlet and at the exit of the propulsor:

$$P_K = \oiint (p_{0_\infty} - p_0)\mathbf{U} \cdot \hat{\mathbf{n}} \, \mathrm{d}S. \tag{3.7}$$

A visual overview of the power balance method is given in Figure 3.2. For a BLI configuration, the net propulsive power is the mechanical flow power minus the jet dissipation ($P_K - \Phi_{jet}$). The wake dissipation is less by a factor of the ingested wake in the engine, f_{BLI}. This results in the following power balance for a BLI configuration

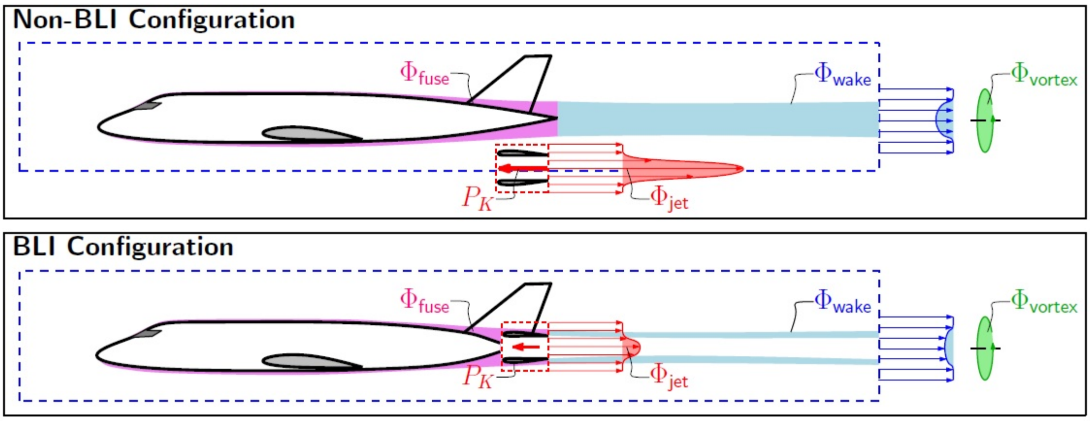

Figure 3.2: Power Balance method, Drela (2009), MIT et al. (2014)

$$P_K - \Phi_{\text{jet}} = \Phi_{\text{fuselage}} + (1 - f_{\text{BLI}})\Phi_{\text{wake}} + \Phi_{\text{vortex}}. \tag{3.8}$$

For the non-BLI case the jet dissipation, Φ_{jet}, and the wake dissipation, Φ_{wake} are higher than for a BLI configuration, with the fuselage dissipation, Φ_{fuselage}, approximately the same.

3.1.2 System-level Advantages of BLI

The various system level benefits of BLI are configuration specific. Detailed (system-level) advantages for the D8 were given in Section 2.2.

- BLI uses an integrated configuration and less structure will be needed compared to a non-integrated configuration. The pylon structure can be removed and the nacelles reduced, resulting in a reduction in weight and wetted surface area and thus a reduction in drag. According to Lord et al. (2000) external nacelle drag can contribute on the order of 3-5% to the total aircraft drag.
- A BLI configuration has a lower power requirement, enabling lower thrust engines, reducing weight.
- Having the engines at the rear of the fuselage (to ingest the largest boundary layer), reduces the engine-out yaw moments, enabling decreased vertical tail area, and weight reduction. (Drela (2011))

- The propulsion system is shielded, resulting in a noise reduction. Lighthill (1952) showed that the jet noise scales with the eighth-power of the jet velocity. The noise is further reduced by the reduced exit velocity. However the noise might increase by ingesting distorted flow.
- Having the engines placed at the back of the aircraft will result in less bird strike.

3.2 Defining the Benefit

The BLI benefit depends on the metric and the method of comparison. This section discusses the different metrics of comparison, the considerations in choosing a method of comparison and the BLI benefits found for the D8 aircraft.

3.2.1 Metric of Comparison

Many metrics of comparisons have been used to assess the BLI benefit. Lynch (1960) used the thrust specific fuel consumption (SFC), the ratio of the fuel mass flow rate to the net thrust. The thrust is not the best parameter to assess the BLI benefit, because for a BLI configuration the thrust required to propel the same body may be lower than for a non-BLI configuration, resulting in a higher SFC. The most used metric of comparison is the propulsive efficiency, η_p, defined by the ratio of useful work to work added to the stream. The problem with propulsive efficiency is that for BLI the propulsive efficiency can become bigger than unity. This can be explained by looking at the power balance method from Drela (2009), as given in Section 3.1.1. The kinetic energy consumption is the sum of the boundary layer dissipation, Φ_{BL} and the energy out flux of the wake, $E_{w,body}$. The energy input from the propulsor has to balance the boundary layer dissipation, Φ_{BL}, resulting in the following formula for the propulsive efficiency (Lv and Rao (2013))

$$\eta_{p,\text{BLI}} = \frac{TU_\infty}{E_p} = \frac{DU_\infty}{E_{p,\text{BLI}}} = \frac{\Phi_{\text{BL}} + E_{w,\text{body}}}{\Phi_{\text{BL}}} \tag{3.9}$$

in which T is the thrust, U_∞ the free stream velocity, E_p the kinetic energy of the propulsor, Φ_{BL} the viscous dissipation of the boundary layer, and $E_{\text{w,body}}$ the kinetic energy of the body wake. Equation 3.9 will clearly be larger than one. This would mean that the useful work would be larger than the work added, which cannot be the case.

A better way to define the BLI benefit is to use the power saving constant (PSC), first defined by Smith (1993), but used in a modified way in this report, Equation 3.10

$$\text{PSC} \equiv \frac{P_{K\,\text{non-BLI}} - P_{K\,\text{BLI}}}{P_{K\,\text{non-BLI}}} \tag{3.10}$$

where P_K is the defined by Equation 3.7 for incompressible flow.

Having defined a metric of comparison, the method of comparison has to be decided.

3.2.2 Method of Comparison

Uranga et al. (2014) and Huang (2014) showed that comparisons of BLI and non-BLI can be made in many ways: equal (inlet/exit) area, mass flow, pressure rise, thrust or power, horizontal force, and/or velocity or combinations of these. These factors all cannot be held constant in a comparison, because these are all dependent on each other. The velocity, for example, is highly correlated with the mass flow, pressure rise and area.

Huang (2014) summarized this in Figure 3.3, giving P_K versus the area ratio $A_{\text{jet}}/A_{\text{BLI}}$ for BLI and non-BLI, indicating different ways of matching, with P_k defined by Equation 3.7. In this Figure the net stream-wise force, F_X, is kept zero, representing cruise condition. Comparing at the same power, P_K, the non-BLI configuration would require a 1.5 times larger nozzle, increasing the size and weight of the aircraft. The same nozzle area requires about 7% more power for non-BLI. The same mass flow requires 8% more power. This example illustrates the issues in comparing BLI configurations with a non-BLI configurations.

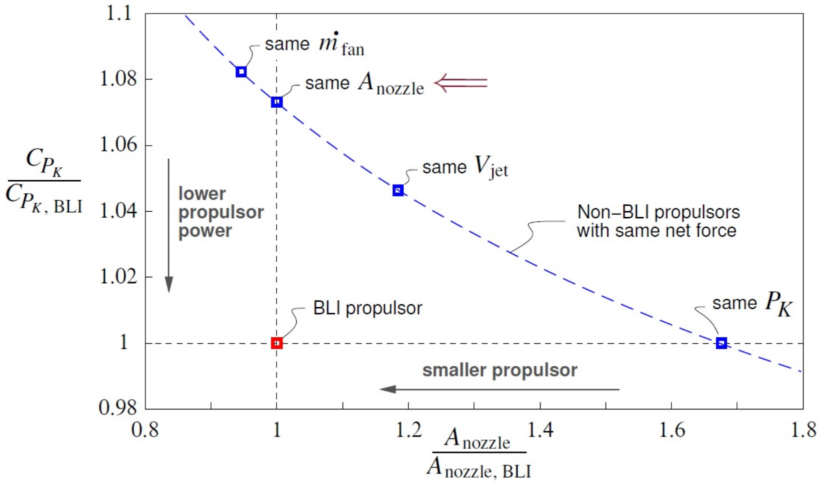

Figure 3.3: BLI versus non-BLI comparison at zero stream-wise force, Uranga et al. (2014)

For the D8 aircraft equal nozzle area, at zero net stream-wise force, F_X, is chosen to assess the BLI benefit.

3.3 BLI Benefit D8 Aircraft

The BLI benefit at cruise condition for the D8 aircraft has been determined using three different methods.

1. **Direct measurement**: P_K is calculated from direct flow integration. The inlet and exit of the propulsor are surveyed with a five hole probe to determine the pressure difference. Static pressure measurements are performed to determine the flow velocity. P_K is calculated by

$$P_K = \iint_{\text{exit}} (p_0 - p_{0_\infty})\, \mathbf{V} \cdot \hat{n}\, d\mathrm{S} - \iint_{\text{inlet}} (p_0 - p_{0_\infty})\, \mathbf{V} \cdot \hat{n}\, d\mathrm{S} \tag{3.11}$$

   At the time this thesis was written the post-processing of the data was not finished.

2. **Indirect measurement**: The electrical power, P_E, is measured by measuring the voltage, v, and current, i, of the power supply. The electrical power, P_E, is related to the mechanical power by the fan efficiency, η_f, and the motor efficiency, η_m:

$$P_K = \eta_f \eta_m P_E \tag{3.12}$$

   This gave a BLI benefit of (MIT internal (2015)):

   - *8.4% BLI benefit (±0.7%)* at equal nozzle area ($\mathrm{A}_{\text{nozzle}}$)
   - *10.5% BLI benefit (±0.7%)* at equal mass flow ($\dot{m}$)

   The uncertainty of ±0.7% comes from uncertainties in the force balance, power supply and tunnel instruments.

3. **Numerical simulations**: Pandya et al. (2014) used Chimera Grid Tool to create the grid, Overflow 2.2 as solver and an actuator disc model for the propulsors, see Section 4.2. The results are displayed in terms of the mechanical flow power coefficient, C_{P_K}, $(P_K/q_\infty U_\infty S_{\text{ref}})$. A *BLI benefit of 9%* is calculated in terms of PSC, as can be seen in Figure 3.4, displaying the power versus the stream-wise force.

An overview of the BLI benefit at cruise obtained by the three methods is given in Figure 3.5, giving the net force coefficient versus the net flow power coefficient. A zoomed view of the lines crossing C_X=0 (cruise) is given on the right of this figure. All curves lie close to each other and the distance between each pair of curves is approximately the same, giving a *±8% BLI benefit*.

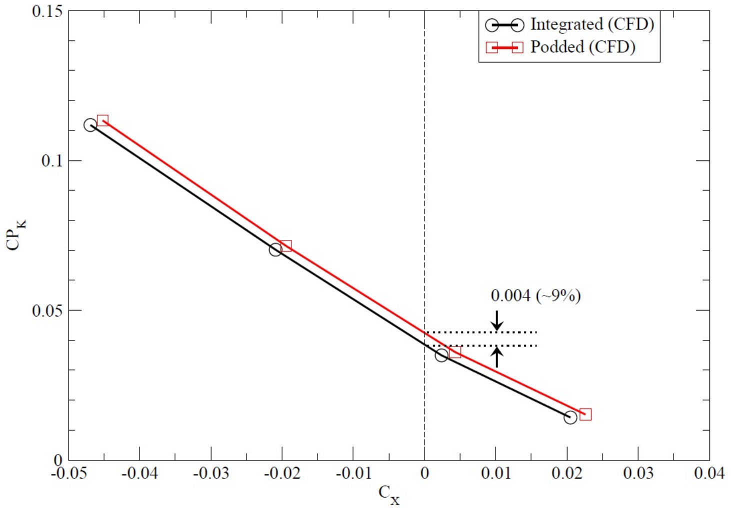

Figure 3.4: C_{P_K} versus net force coefficient, C_X, Pandya et al. (2014)

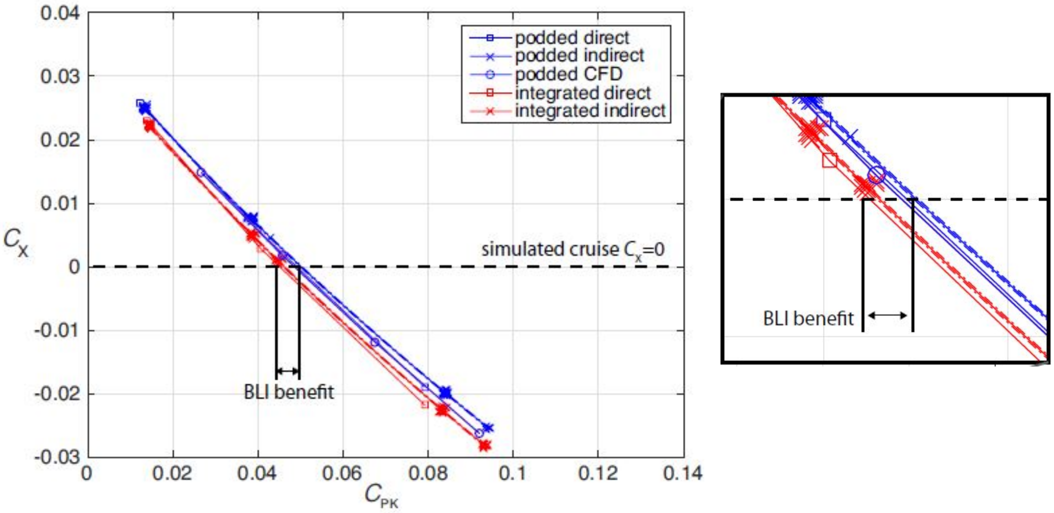

Figure 3.5: Aerodynamic BLI benefit, combined results, MIT internal (2015)

3.4 BLI Assessment

The BLI benefit found in literature is presented in Appendix A. The BLI benefit ranges from no benefit to 70% benefit (including system level advantages), depending on the metric and method of comparison and whether aerodynamic losses were taken into account. The most important BLI assessments were performed by Lynch (1960) and Smith (1993), and are given in this section.

Lynch (1960) was the first to identify that the wake momentum defect is reduced by an amount equal to the momentum defect of the air taken into the inlet. However, he did not place the propulsor such that the outflow of the propulsor would be in the wake of the airframe, as can be seen in Figure 3.6. Referring back to the power balance, he identified a reduction in wake dissipation, contributing to a BLI benefit of about 3% in terms of SFC, the ratio of the fuel mass flow rate to the net thrust.

Lynch (1960) derived the equations for the thrust, F_n, with BLI (prime) and without BLI (no prime), and applied his analysis to the (specifications of the) JT3D turbofan engine, a low-bypass-ratio engine of Pratt&Whitney (Pratt & Whitney (b)), and the JT3C turbojet engine (Pratt & Whitney (a)). For steady level flight, the thrust, F_n is given by Equations 3.13 and 3.14.

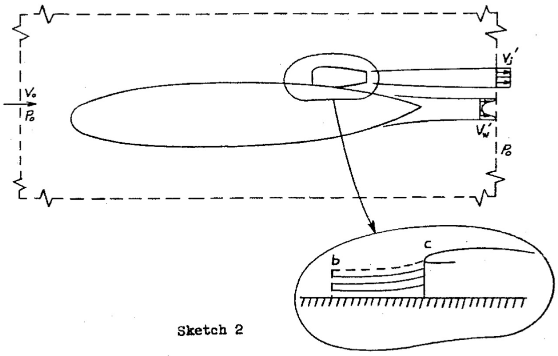

Figure 3.6: Boundary layer ingestion sketch by Lynch (1960)

$$F_n = \frac{\dot{m}}{g}(U_j - U_0) \tag{3.13}$$

$$F_n' = \frac{\dot{m}'}{g}(U_j' - \overline{U}_{\text{B.L.}}) \tag{3.14}$$

where $\dot{m}$ is the engine airflow, g the acceleration of gravity, U_j the jet velocity, U_0 the free stream velocity, and $U_{\text{B.L.}}$ the velocity of the boundary layer, evaluated upstream of the engine to not capture the engine interaction.

Lynch (1960) used the momentum averaged velocity of the boundary layer to define the boundary layer velocity, as given in Equation 3.15.

$$\frac{\overline{U}_{\text{B.L.}}}{U_{\text{L}}} = \frac{\frac{(mU)_{\text{B.L.}}}{(mU)_{\text{L}}}}{\frac{(m)_{\text{B.L.}}}{(m)_{\text{L}}}} \tag{3.15}$$

$$\frac{(mU)_{\text{B.L.}}}{(mU)_{\text{L}}} = \frac{1}{\beta}\int_0^\beta \frac{\rho U^2 \, \mathrm{d}y}{\rho_{\text{L}} U_{\text{L}}^2} \tag{3.16}$$

The results of this investigation can be seen in Figures 3.8 and 3.9, giving the SFC versus the thrust, where the definitions of the parameters are given in Figure 3.7. β is the portion of the boundary layer taken into the inlet, y the distance from the surface

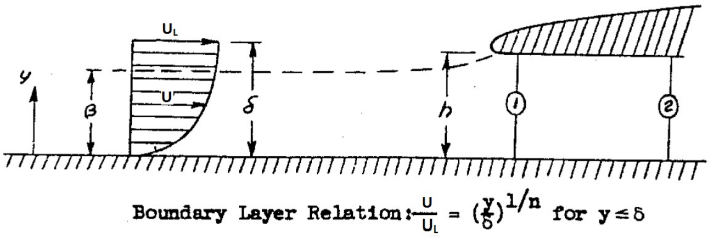

Figure 3.7: Nomenclature, Lynch (1960)

in vertical direction, h the inlet height, δ the boundary layer height, U the velocity, U_L the velocity at the edge of the boundary layer, n the number used in the boundary layer relation, and RRR the ram recovery ratio. $\Delta p_t/q$ represents the internal inlet loss, where P_t is defined as the total pressure, and q_1 the dynamic pressure at the inlet station.

For the JT3D turbofan, Figure 3.8, Lynch (1960) found that SFC reductions of about 3% are theoretically possible at cruise conditions (M =0.825, Alt = 10668 [m], F_n'=17800 [N]), using an h/δ of 1.5 (66% BLI). When the inlet losses become higher ($\Delta p_t/q$=0.15), the use of BLI increased the SFC by about 1% when ingesting 50% of the boundary layer.

For the JT3C turbojet engine, Figure 3.9, at cruise conditions, h/δ of 1.5 would increase SFC, so there would be no BLI benefit.

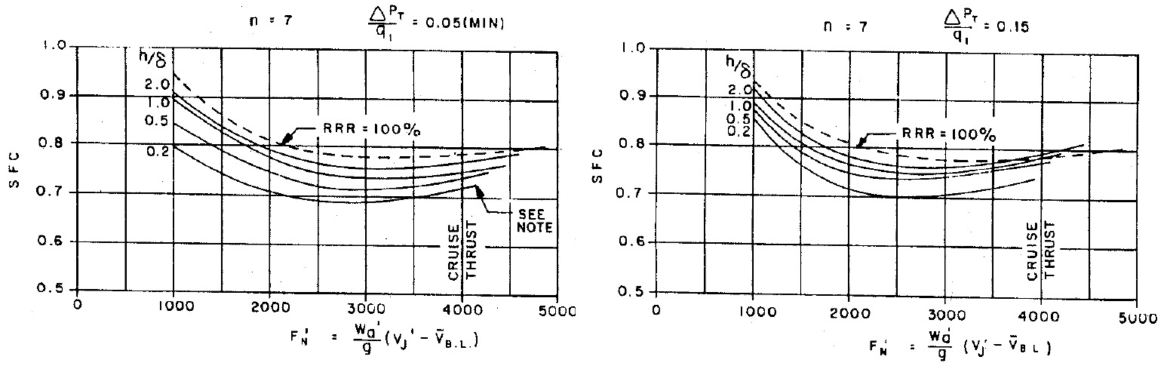

Figure 3.8: JT3D, turbofan, M=0.825, Alt=10668 [m], $\Delta p_t/q$=0.05 (left), $\Delta p_t/q$=0.15 (right), (note=cut-off point represents max. continuous power setting), Lynch (1960)

Lynch (1960)'s conclusion was that further investigation of BLI was not worthwhile, because the small (3%) reduction in SFC under ideal circumstances would not compensate the practical implementation problems and possible aerodynamic losses.

The analysis of Lynch (1960) is of value, because he identified that the wake momentum is reduced equal to the amount of BLI ingested in the inlet and that ingesting more of

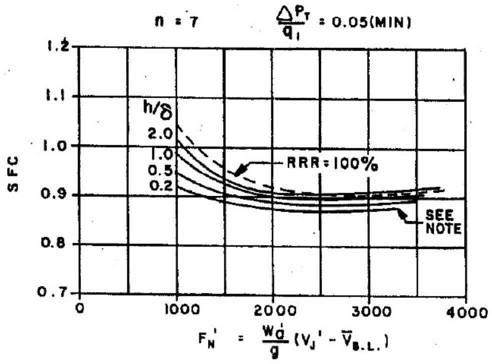

Figure 3.9: JT3C Turbojet, M=0.825, Alt=10668 [m] (note=cut-off point represents max. continuous power setting), Lynch (1960)

the boundary layer is beneficial, because that would change the thrust required. This is in accordance with theory developed by Smith (1993). He also identified the fact that BLI does not 'work' for turbojet engines, because the compressor should get air with the highest possible total pressure, so free stream air.

Smith (1993) assessed the BLI benefit using an actuator disc model of a propulsor. He compared the power input to achieve a certain thrust for a BLI propulsor disc with a propulsor that ingests uniform flow. The flow geometry is shown in Figure 3.10. The thrust and power of the non-BLI case are given by Equations 3.17 and 3.18

$$T = \dot{m}(U_j - U_0) = \frac{\rho}{2}A\left(U_j^2 - U_0^2\right), \tag{3.17}$$

$$P = \dot{m}\left\{\left(\frac{U_j^2}{2}\right) - \left(\frac{U_0^2}{2}\right)\right\} = \frac{1}{2}T(U_j + U_0). \tag{3.18}$$

For BLI the thrust is the sum of the momentum change of the wake and the non-wake streams, resulting in Equations 3.19 and 3.20.

$$T_{\text{BLI}} = \rho(A - \delta_p)\frac{U_j + U_0}{2}(U_j - U_0) + \rho\int^{\delta} U_w(U_{jw} - U_w)\,\mathrm{d}A \tag{3.19}$$

$$P_{\text{BLI}} = \rho(A - \delta_p)\frac{U_j + U_0}{2}\frac{U_j^2 - U_0^2}{2} + \rho\int^{\delta} U_w\frac{U_{jw}^2 - U_w^2}{2}\,\mathrm{d}A \tag{3.20}$$

In Equations 3.17, 3.18, 3.19 and 3.20, $\dot{m}$ is the mass flow rate through the propulsor, U_0 is the flight velocity, U_j the axial velocity in the jet (the velocity in free stream flow direction), U_{jw} the jet velocity in the wake, A the propulsor disc area, and δ_p the wake area at the propulsor disc, as can be seen in Figure 3.10.

Smith (1993) used a power saving coefficient (PSC), as defined in Section 3.2.1 to model the BLI benefit. His PSC is given in Equation 3.21. It is related to the wake form factor, H, the thrust loading coefficient, C_{th}, and the wake recovery ratio, R, as

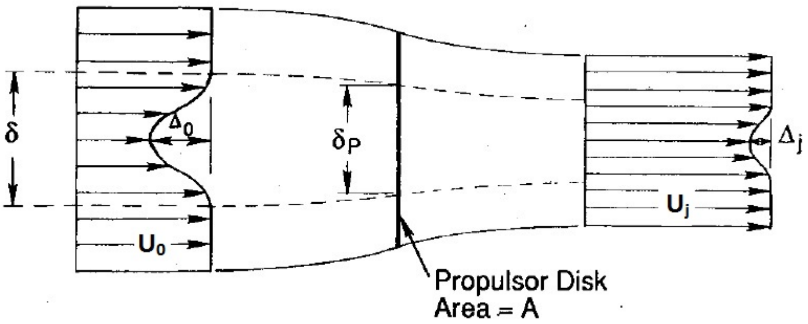

Figure 3.10: Actuator disc model, propulsor ingesting wake, Smith (1993)

given in Equations 3.22, 3.23, and 3.24, where K is the pseudoenergy factor, given by Equation 3.25.

$$PSC = \frac{U_j' - U_j}{U_j' + U_0}\frac{T}{D} + \frac{U_0(2-R)}{U_j' + U_0}\left[\frac{U_j}{U_0} - 1 + R(1-K)\right] \tag{3.21}$$

$$H = \frac{\delta^*}{\theta} = \frac{\int^{\delta}\left(1 - \frac{U_w}{U_0}\right)\mathrm{d}A}{\int^{\delta}\frac{U_w}{U_0}\left(1 - \frac{U_w}{U_0}\right)\mathrm{d}A} \tag{3.22}$$

$$C_{\mathrm{th}} = \frac{T}{\frac{1}{2}\rho U_0^2 A} \tag{3.23}$$

$$R = 1 - \frac{\Delta_j}{\Delta_0} = 1 - \frac{U_j - U_{jw}}{U_0 - U_w} \tag{3.24}$$

$$K = \frac{k}{\theta} = \frac{\int^{\theta}\frac{U_w^2}{U_0^2}\left(1 - \frac{U_w}{U_0}\right)\mathrm{d}A}{\int^{\delta}\frac{U_w}{U_0}\left(1 - \frac{U_w}{U_0}\right)\mathrm{d}A} \tag{3.25}$$

The dependence of the PSC on the thrust loading coefficient, C_{th} is seen in Figure 3.11. Here the wake recovery factor is kept constant at 0.8, meaning that the wake is not totally flattened. The PSC increases with increasing wake form factor, H, and with increasing thrust loading coefficient, C_{th}. The conclusion is that high disc loading and high form factors are favorable, but the main influence is the wake shape factor, H.

The dependence of the PSC on the wake recovery factor, R, can be seen in Figure 3.12. The closer the wake recovery is to 1, the higher the PSC. Figure 3.13 gives the relation between the propulsive efficiency and ratio of the disc area to wake area. The larger the ratio of disc area to wake area, the higher the propulsive efficiency; ingesting more boundary layer is beneficial. The PSC for the ideal case is given in Figure 3.14, displaying the relation between the PSC and the wake form factor. A PSC of up to *25%* can be achieved for a form factor, H, of 2.

Smith (1993) also determined the influence of the local advance coefficient, ϕ, defined by the ratio between the flight velocity to the local blade velocity, on the wake

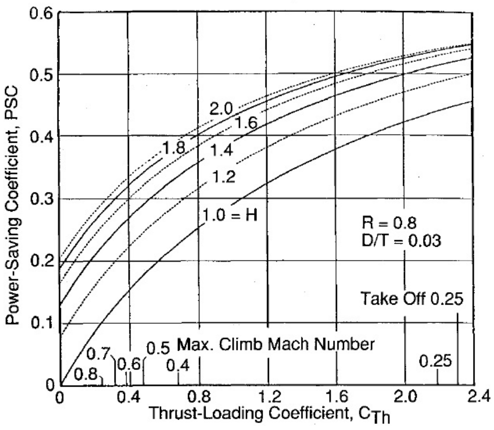

Figure 3.11: Effect of disc loading and wake form factor, Smith (1993)

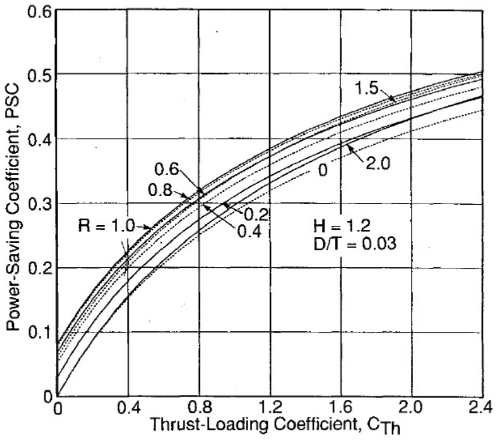

Figure 3.12: Effect of wake recovery, Smith (1993)

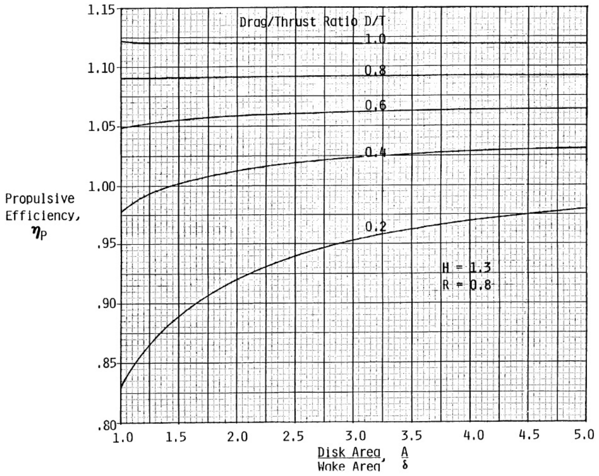

Figure 3.13: Effect of propulsor size, Smith (1993)

recovery ratio is evaluated. The influence of the advance ratio on the wake recovery is given by Equation 3.26.

$$R = 1 - \frac{2\phi + (\mathrm{d}C_T/\mathrm{d}\phi)}{2\sqrt{\phi^2 + C_T}} \tag{3.26}$$

Figure 3.15 shows that the wake recovery decreases with increasing advance coefficient. It is advantageous to have low ϕ, meaning that the blade speed, U should be high relative to the flight velocity.

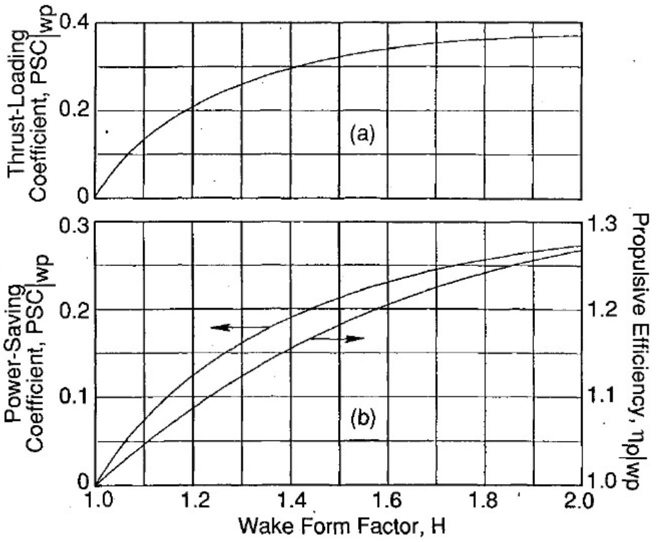

Figure 3.14: Wake propulsion ideal case, Smith (1993)

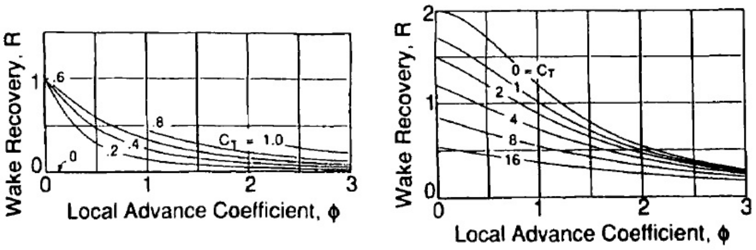

Figure 3.15: R versus ϕ, single-rotation propeller blade elements (left), and high solidity counter-rotating propeller elements (right), Smith (1993)

The conclusions drawn by Smith (1993) are

- The propulsor should be positioned such that it ingest the stream with a high form factor, H. The form factor is defined by the ratio between the wake displacement area and the wake momentum area. When the wake moves downstream, shear stresses can flatten the wake, reducing the form factor, and lowering the PSC.
- The propulsive efficiency η_p increases with increasing D/T, where D/T equals 1 means that all the wake passes through the propulsor.
- A wake recovery ratio, R, as close as possible to 1 is desired for highest efficiency, where the case R=1 corresponds to a totally flattened wake.
- At high advance coefficients (ϕ), the wake recovery, R, is poor. It is beneficial to have R as close as possible to 1. To have a low advance coefficient, the local bleed speed, U, should be high, relative to the flight velocity.
- High disk loading, or high thrust loading coefficients, C_{th}, are favorable.

These conclusions are regarded as the most important guidelines for optimizing a BLI configuration. The real BLI benefit depends on the (aerodynamic) losses, which as Lynch (1960) identified, could eliminate the BLI benefit. These losses are mainly caused by ingesting a non uniform velocity, causing inlet pressure distortions, explained in the next section.

3.5 Inlet Pressure Distortions

A conventional configuration, Figure 3.16, has a uniform inflow and the inflow is independent on the shape of the aircraft and the flight condition. A BLI configuration, Figure 3.17, ingests the boundary layer, resulting in a non-uniform velocity at the fan-face. The inflow is dependent on the aircraft geometry, placement of the propulsor, and flight condition. The performance of the propulsor has to be assessed as part of an aircraft configuration and for different mission points.

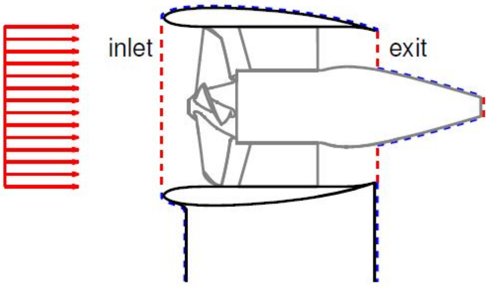

Figure 3.16: Uniform inflow velocity (non-BLI)

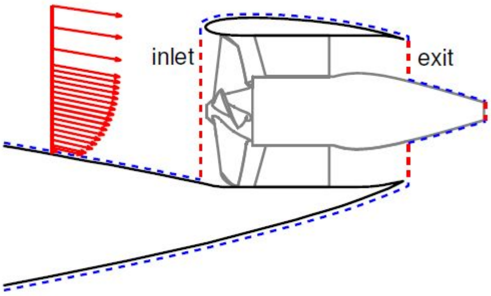

Figure 3.17: Non-uniform inflow velocity (BLI)

The consequences of the non-uniform (total) pressure distribution at the propulsor inlet are possible performance degradations, unsteady blade forces, vibration and a reduction in stall margin (Boller (1998)).

Kimzey (1977) modeled the influence of inlet total pressure distortions on stability for a XC-1 compressor, by varying the distortion in a 60° sector, located on the bottom of the inlet as illustrated on the right of Figure 3.18, He compared the results to experiments. The result is given in Figure 3.18, where N is equal to the compressor rotor speed, P the total pressure, W the circumferential velocity component in three-dimensional model development, δ the ratio of compressor entry total pressure to standard day, sea level static pressure. Increasing the strength of the pressure distortion reduces the stall margin of the compressor.

Mehalic (1988) experimentally determined the effect of inlet pressure distortions on the stability of a PW1128 turbofan engine. The pressure distortion was produced by a screen installed in the inlet ducting between the burner and the engine inlet. The result is given

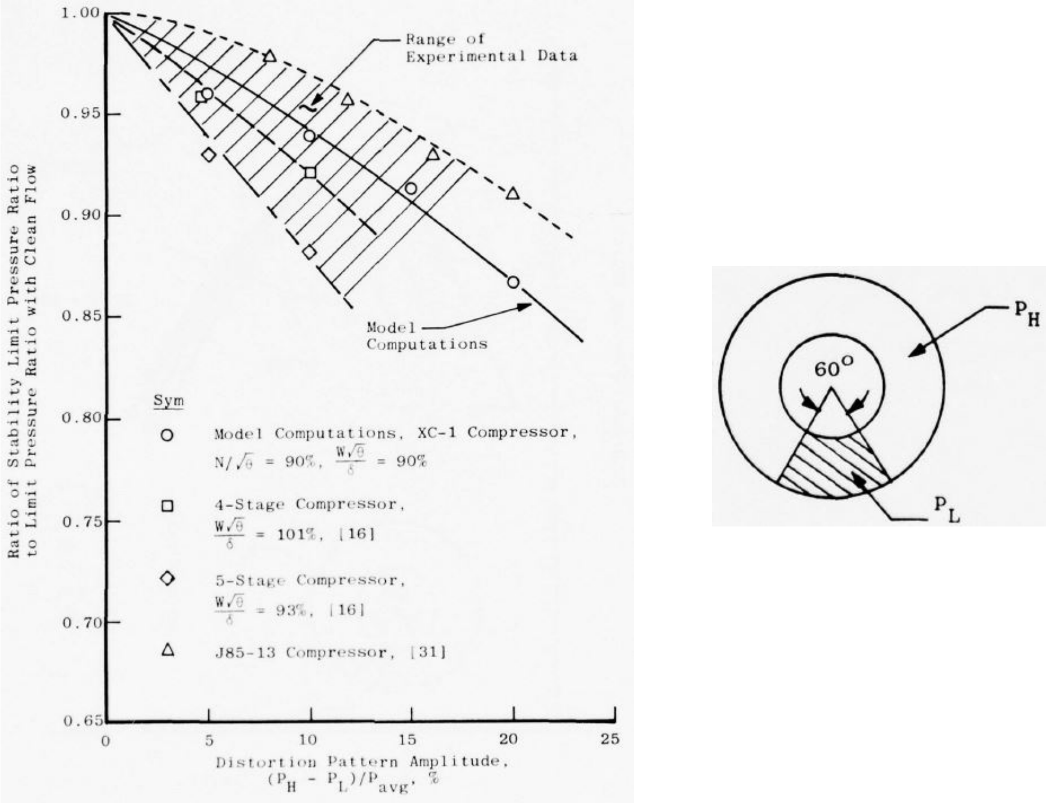

Figure 3.18: Model computed influence of circumferential pressure distortion on stability, comparison with experimental results, Kimzey (1977)

in Figure 3.19, where N_1 is the fan rotational speed, θ the ratio of total temperature to absolute temperature of standard sea level conditions, W the gas flow rate and δ the ratio of total pressure to absolute pressure of standard sea level conditions. At 90.2 percent corrected fan speed, the total pressure distortion resulted in a 6.2 percent loss of stall pressure ratio. The effect of the pressure distortion at 100.2 percent corrected speed was an 8.3 percent loss in stall pressure ratio.

The research by Mehalic (1988) and Kimzey (1977) clearly demonstrate the importance of determining the inlet distortion. Much research has been performed on the (total pressure) inlet distortions for Hybrid Wing Body (HWB) aircraft, Figure 3.21. HWB use serpentine-ducts (S-ducts), Figure 3.20, to guide the flow in the propulsors, which have an elongated s-shape. This turning of the flow causes distortions and pressure losses, such that the distortions found are not solely related to boundary layer ingestion. The D8 aircraft does not make use of a S-duct. The next chapter will describe the methods used to assess the inlet distortions for the boundary layer ingesting D8 aircraft at various flight conditions.

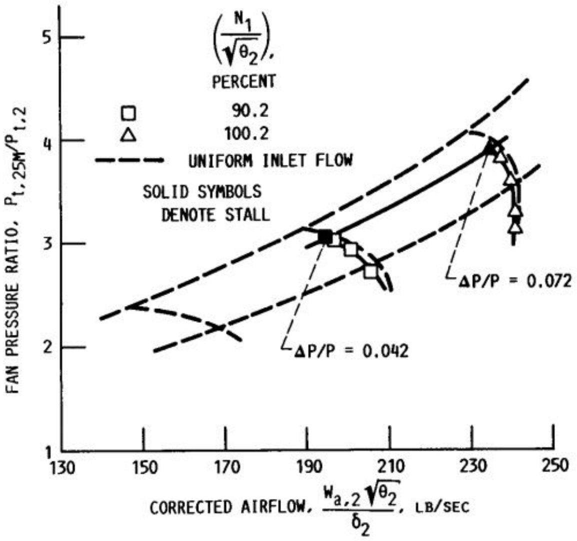

Figure 3.19: Effect of circumferential inlet total pressure distortion on fan stability, Mehalic (1988)

Figure 3.20: Serpentine Inlet (S-Duct), Ferrar et al. (2009)

Figure 3.21: Hybrid Wing Body (HWB)

Chapter 4

Methodologies

This chapter describes the experimental and computational methods used to assess the inlet distortions, and the post-processing of these. At the end of this chapter the most important mission points of the D8 are described.

4.1 Experimental Assessment

The method to assess the flow in the vicinity of the engines should not affect or interact with the propulsors, such that use of surface oil flow visualization, the application of oil on the surface of the wind tunnel model, and smoke flow visualization, are not preferred. Particle image velocimetry (PIV), the measurement of velocity fields by taking two subsequent images of a plane and calculating the direction and distance the particles have traveled, requires particles (seeding) in the wind tunnel, which could also affect the propulsor performance. It has been chosen to use mini-tufts flow visualization in combination with five hole probe measurements at the propulsor inlet.

To execute these methods a D8 wind tunnel model and a wind tunnel are needed. The key performance parameters are matched; overall similar L/D of 21, similar fraction of ingested kinetic energy defect, f_{BLI}, and similar jet velocity ratios, $V_{\mathrm{jet}}/V_{\infty}$.

4.1.1 Wind Tunnel Model

A 1:11-scale D8 wind tunnel model was built in cooperation with Aurora Flight Sciences (Sciences). The model has three different tail configurations, a podded configuration, a powered integrated configuration and an unpowered integrated configuration. An overview of the different configurations is given in Figure 4.1, and specifications are given in Table 4.1. The podded and integrated configuration have 80% of the fuselage in common, including the same wings and propulsor units, enabling a back-to-back comparison of a BLI configuration with a non-BLI configuration, such that the BLI benefit can be assessed. For the determination of the inlet distortions only the powered integrated configuration is considered.

Use is made of carbon-composite TF8000 ducted fans, manufactured by Aero-naut. The rotor has 5 blades, and the stator 4 blades. Each propulsor has a 2 kW Lehner Motor 3040-27 brushless DC electric motor (Lehner), and is powered by a Sorensen 2 kW DC power supply with a 240 V, 3-phase, input (Ametek Programmable Power).

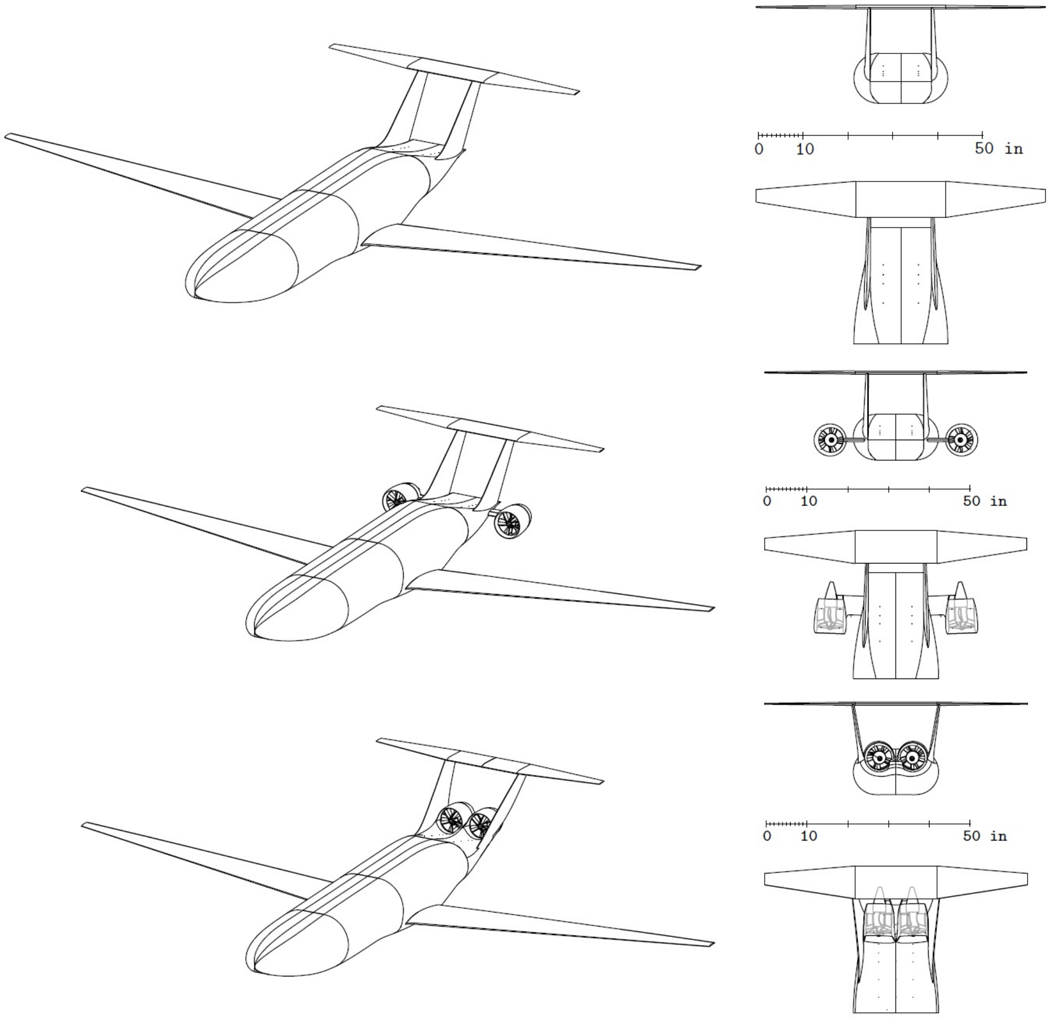

Figure 4.1: Unpowered (top), podded (middle), and integrated (bottom) configurations, Uranga et al. (2014)

Table 4.1: Reference dimensions of the 1:11 scale D8 model

Dimension	Value
Reference Area S_{ref}	1.088 m^2
Reference chord c	0.273 m
Span	4.097 m
Overall length (integrated)	3.218 m
Propulsor fan diameter	0.144 m

4.1.2 Wind Tunnel

The 14x22 foot Subsonic Wind tunnel at NASA Langley was used, which is a closed circuit wind tunnel with a large test section. A picture of the 1:11 scale D8 wind tunnel model in the 14x22 foot Subsonic Wind tunnel is presented in Figure 4.2, the specifications are given in Table 4.3 and the operating conditions for this test is given in Table 4.2. The experiments are performed at low speed as the BLI benefit is not explicitly dependent on Mach number or Reynolds number (Uranga et al. (2015)). The size of the model is small compared to the size of the wind tunnel test section. Therefore it is assumed that the model blockage and wind tunnel wall effects (corrections were estimates) will have a minimal influence on the propulsor inlet pressure distribution and surface streamlines (Dietz and Laster (1981)). Also corrections related to the use of a powered configuration are assumed to not be of influence on the inlet pressure distribution and surface streamlines upstream of the propulsor (Ewald (1998)).

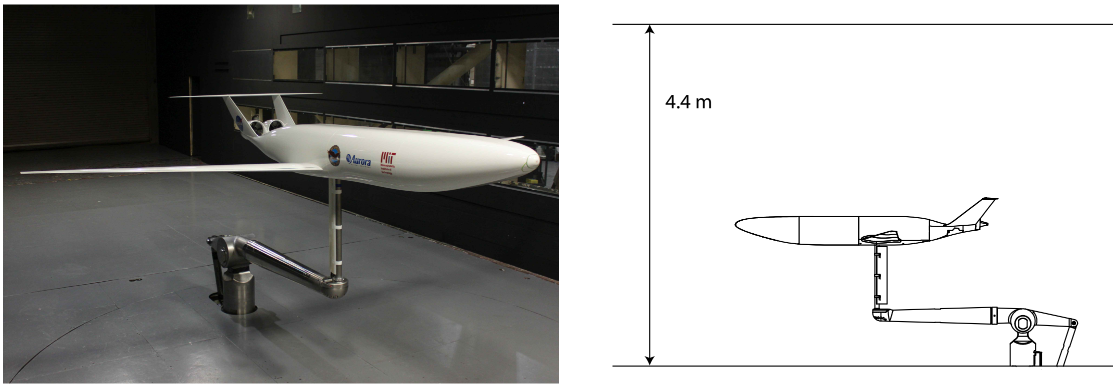

Figure 4.2: 1:11 scale D8 model in the 14x22 ft Subsonic Wind tunnel at NASA Langley

Table 4.2: Tunnel nominal operating conditions (standard sea level)

V_∞ [ms^{-1}]	q_∞ [Pa]	M_∞	Re_c
18.8	216	0.055	3.6 x 10^5
31.3	598	0.0092	5.7 x 10^5
37.6	864	0.11	7.0 x 10^5

Table 4.3: Specifications 14x22 ft. Subsonic Wind tunnel NASA Langley, NASA (a)

Speed	0-106 ms^{-1}
Test section	4.4 H x 6.6 W x 15.2 L m
Circuit length	234.7 m
Contraction area ratio	9:1

4.1.3 Mini-tuft Flow Visualization

Mini-tuft flow visualization is used to assess the flow upstream the propulsors and on the propulsor nacelles. Mini-tufts are filaments of white polyester monofilament thread, which are attached to a wind tunnel model and follow the flow when the wind tunnel is running. These filaments do remain attached to the surface during the test and therefore do not affect the propulsor performance. A camera is used to capture the result. The diameter and length of the tufts should be large enough for the camera to capture the tufts, but small enough to follow the flow accurately. Barlow et al. (1999) suggests a tuft length of 19 mm. The results will also give information on unsteady flow, which is displayed as blurred tufts, and on the flow direction.

4.1.4 Five Hole Probe Surveys

A five hole probe was used for flow measurements at a plane as close as possible to the propulsor fan-face. The probe has to be placed upstream of the body, such that the probe interference is negligible. The probe, displayed in Figure 4.3, was custom made by the AeroProbe Corporation. It has a tip diameter of 1.6 mm resulting in minimal flow disturbance. The five hole probe has an average measured angular deviation of less than 1° and an average measured velocity deviation of 1% or ±1ms^{-1}.

The use of five hole probes close to a surface could decrease the accuracy of the probe. Tamigniaux and Gordon (1986) performed experiments with a five hole probe close to a flat plate, and concluded that the probe can be used in the proximity of a wall, if this is taken this into account during calibration. The wall interference would mainly cause an increased pressure at port 2, Figure 4.4, leading to an increase in estimated angles. Lee and Yoon (1999) determined the wall effect of a five hole probe for various probe-wall orientations, varying the yaw angle. They found that the wall-proximity effect was only pronounced when the distance was less than two times the probe-head diameter. In this experiment a probe head diameter of 1.6 mm is used. The measurement plane is 11 mm in front of the nacelle on top, 3 mm above the surface, and fixed with respect to the model, illustrated in Figure 4.5. According to Lee and Yoon (1999) the wall effect at 3 mm from the surface with a 1.6 mm probe should thus be negligible.

To execute the probe surveys a grid has to be determined and a traverse system designed to guide the probe to these grid points.

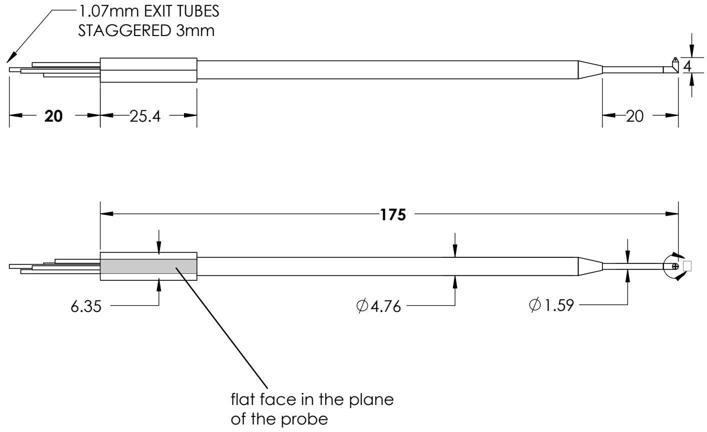

Figure 4.3: Five hole probe, AeroProbe

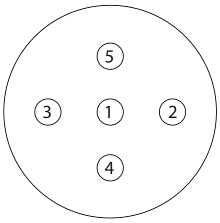

Figure 4.4: Five hole probe pressure ports

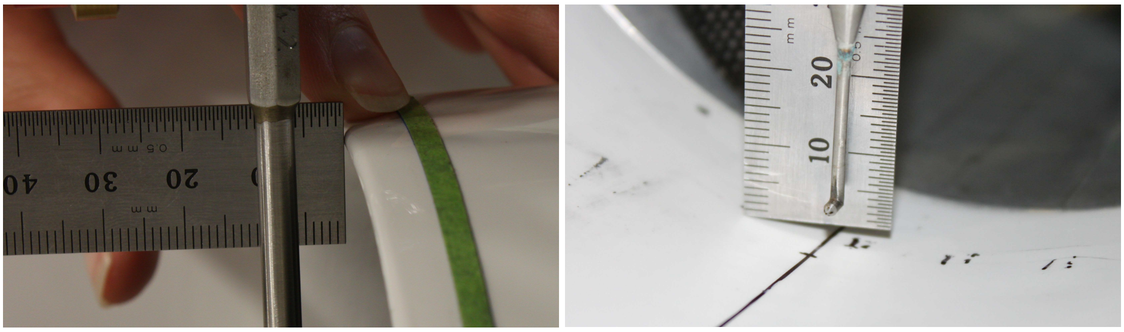

Figure 4.5: Measurement plane five hole probe

4.1.4.1 Grid

The probe has to take measurements at a large number of grid points to obtain the pressure distribution at a high resolution. Use has to be made of an optimal grid to reduce the test time per condition. The grid is dense in regions where flow features of interest are expected, to reduce the number of grid points. The regions of interest are on the bottom of the propulsor, as illustrated in Figure 4.6, which is the total pressure distribution at the fan-face from CFD.

Two grids were designed, a fine and a coarse grid, to save traverse time. The fine grid, Figure 4.7, is used to get the pressure distribution at the cruise point, has 1852 points and takes around two hours, using a settling time of 2.5 seconds. The coarse grid, Figure 4.8, is used for all other mission points, has 516 points and takes 40 minutes. The grid is extended between the propulsors, towards the vertical tail, and outside the radius of the propulsor to capture flow in these regions. More details on the grid can be found in Appendix B.

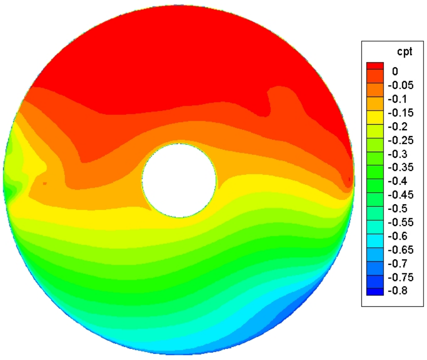

Figure 4.6: Total pressure coefficient (C_{p_t}) at fan-face, cruise condition, CFD

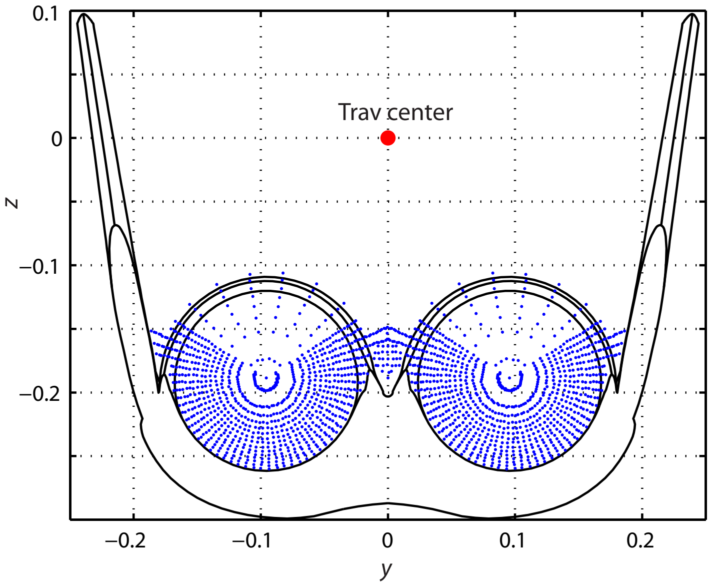

Figure 4.7: Integrated inlet grid, fine

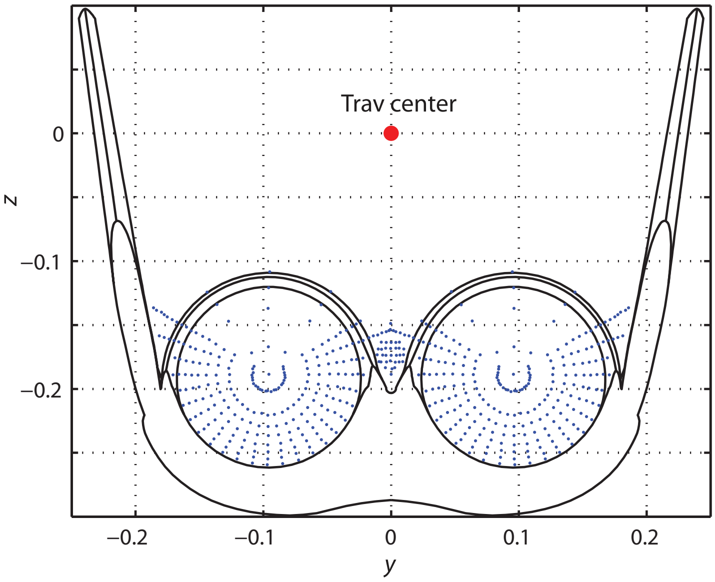

Figure 4.8: Integrated inlet grid, coarse

4.1.5 Traverse System

A mechanical traverse system was designed to move the five hole probe. Figure 4.9 gives a sketch of the wind tunnel model, model support and traverse system. A more detailed view of the traverse is given in Figure 4.10. The traverse system is attached to the model support and model. In this way the measurements are carried out at the correct planes even when the model is under an angle of attack, yawed, or vibrating. There is no structure in front of the five hole probe nor in the measurement plane, resulting in minimal flow distortion.

The system is resting on the propulsor nacelles using two arc shaped pieces that

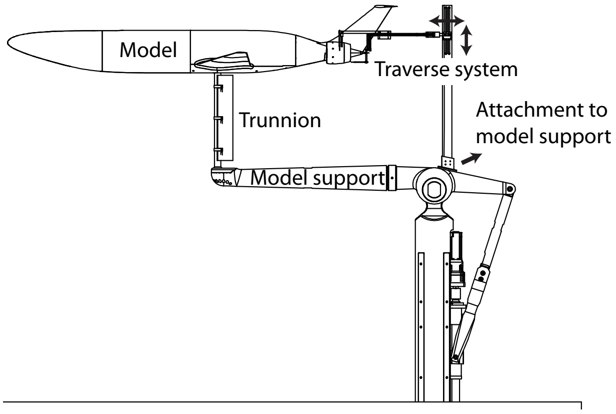

Figure 4.9: Traverse system overview

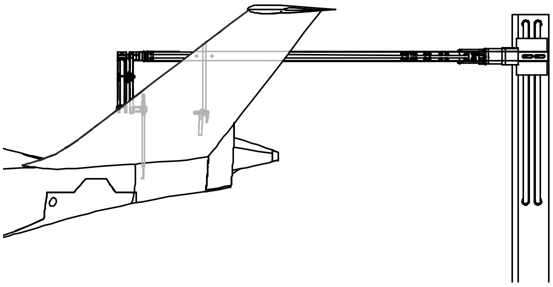

Figure 4.10: Integrated inlet traverse system, side view

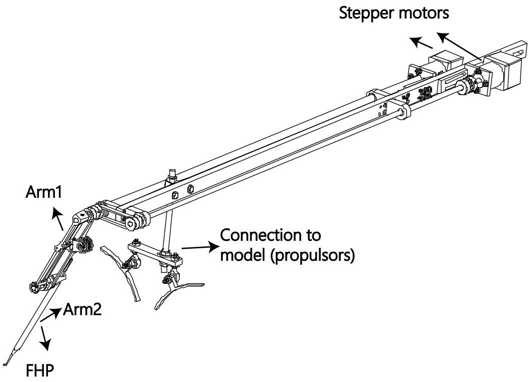

Figure 4.11: Integrated inlet traverse system, detailed view

have the same curvature as the nacelles, as in Figure 4.11. These arcs can be moved up and down to position the traverse. Two stepper motors are used to control the bars that are connected to ball bearings, which are connected to timing belts. The timing belts set the angles of arm1 and arm2. Adjusting the angles of these arms sets the position of the tip of the five hole probe. The stepsize of the stepper motors is 0.45°, such that only a discrete number of points can be reached, this is explained in Appendix B. A picture of the traverse system in the 14x22 foot Subsonic Wind tunnel at NASA Langley can be seen in Figure 4.12.

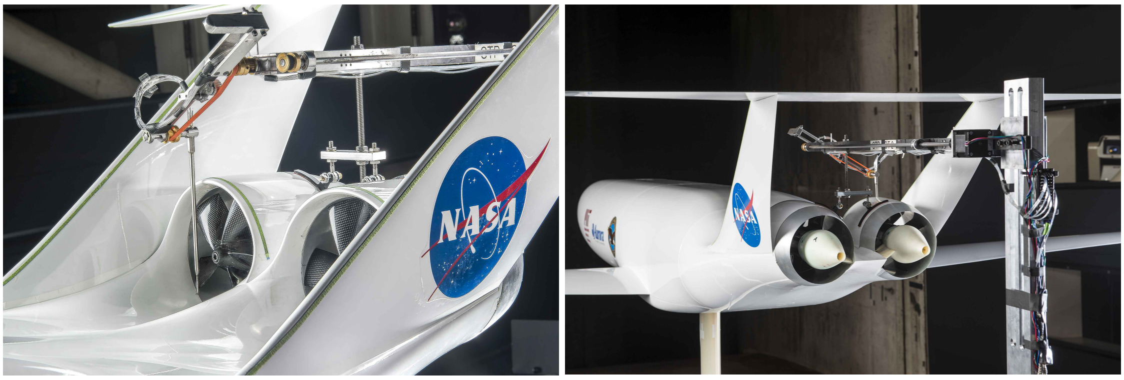

Figure 4.12: Pictures of the front and back view of the traverse system, NASA Langley, photo credit: George Homich

4.2 Computational Assessment

CFD calculations for the D8 have been performed by Shishir Pandya from NASA Ames Research Center (Pandya et al. (2014), Pandya (2015)). He used a 1:11 scale half body, without mounting hardware and inviscid walls, Figure 4.13. The computational mesh was generated by Chimera Grid Tools (Chan et al.). The CFD solver was Overflow 2.2 (Buning), a 3D RANS solver for overset structured grids, using second order central difference, artificial dissipation and RANS SST turbulence model. The computations were performed at a Mach number of 0.088. The propulsors were modeled as an actuator disc, using a uniform pressure jump. Four cases with different pressure jumps were assessed. One was equivalent to the cruise case, it has a horizontal force coefficient, C_X ($F_X/q_\infty S_{\mathrm{ref}}$), close to zero ($C_X$=0.0019), where F_X is the net stream-wise force. One was equivalent to the top of climb condition.

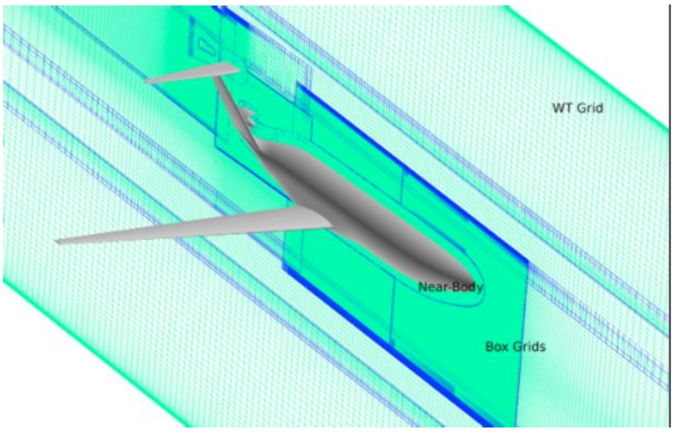

Figure 4.13: 1:11 scale half model, CFD

4.3 Post-Processing

This section describes the post-processing methods used. CFD data at the cruise and top of climb condition is only available for the right side of the model, the results were mirrored to get the left side. This is valid because the model is symmetric and the actuator disc theory does not take into account fan rotation.

4.3.1 Streamlines

Five pictures of the mini-tufts were taken at each condition. The pictures are imported into Adobe Lightroom 5, where an infrared mask is applied and the exposure time and contrast are changed, to make the tufts better visible. Comparing the results for different conditions showed that some tufts were stuck, and should not be taken into account. These are indicated in Figure 4.14.

The CFD data (Pandya (2015)) was imported into Tecplot 360 to generate the surface streamlines. It is not known at what height the mini-tufts capture the flow, therefore streamlines were generated at 4.1 x 10^{-3}, 1.7 10^{-2}, 0.76 and 3.1 mm above the surface.

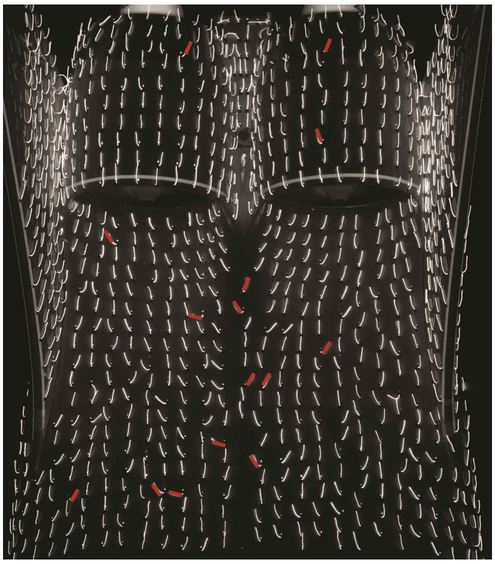

Figure 4.14: Stuck mini-tufts, marked red

4.3.2 Pressure Distribution

The five hole probe has five pressure ports, illustrated in Figure 4.4, to be able to capture the flow angle. At the time this thesis was written the calibration for the flow angles was not yet finished. The pressure value from the middle port (port 1, C_{P_1}) is close to the total pressure value, and is used to assess the distortion. The measured pressure values at each grid point had to be averaged, after which linear scattered data interpolation was used to obtain the pressure values between the grid points.

The CFD data (Pandya (2015)) was imported into Tecplot 360. The total pressure coefficient was computed at a slice 11 mm in front of the top of the nacelle, to compare with the five hole probe measurements.

4.3.3 Distortion Coefficient

A common way to assess the distortions is to calculate the distortion coefficient, DC(θ), given by Equation 4.1 (Seddon and Goldsmith (1999)).

$$\mathrm{DC}(\theta) = \frac{P_f - P_\theta}{q_f} \tag{4.1}$$

where P_f is the mean total pressure at the propulsor face, q_f the dynamic pressure, and P_θ the mean total pressure in the lowest stagnation pressure sector of the face, of angle θ. A sector of 60°, DC(60), is commonly used.

The distortion coefficient was calculated for both propulsors, using a circle of 71.8 mm radius (R_{DC}), equal to the radius of the propulsor, illustrated in Figure 4.15. DC(θ) is calculated from the pressure distribution obtained by the five hole probe measurements, and from the pressure distribution calculated from the CFD data.

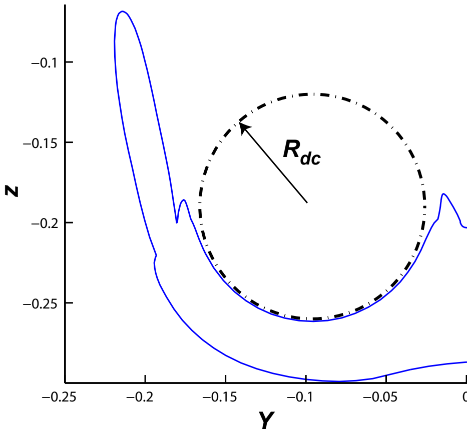

Figure 4.15: Distortion coefficient, conventions

4.3.4 Power Requirement

It is known from the previous wind tunnel experiment at NASA Langley (entry 1) that there is cross-flow present upstream of the propulsors (Uranga et al. (2014)). Both fans rotate in the same direction, as a consequence one has the inflow in the direction of rotation (co-swirl) and one has inflow opposite to the direction of rotation (counter-swirl). This is illustrated in Figure 4.16, where the black arrow demonstrates the direction of the incoming flow. It is expected that this will lead to an unequal power demand for the left and right propulsor.

To assess the power requirement the electrical power, P_E, is measured by measuring the voltage, v, and current, i, of the power supply. The electrical power is converted to the shaft power, P_S, using the motor efficiency. The shaft power coefficient, C_{P_S} is given in Equation 4.2. This is a non traditional way of non-dimensionalizing the shaft power coefficient, used to get a more uniform result for the different flight phases.

$$C_{P_S} = \frac{P_S}{\frac{1}{2}\rho(\Omega R_{\text{tip}})^3 S_{\text{ref}}} \tag{4.2}$$

where P_S is the shaft power supplied to the propulsors, S_{ref} the model reference area (1.088 m^2 at 1:11 scale), Ω the angular velocity, R_{tip} the tip radius, equal to 71.8 mm.

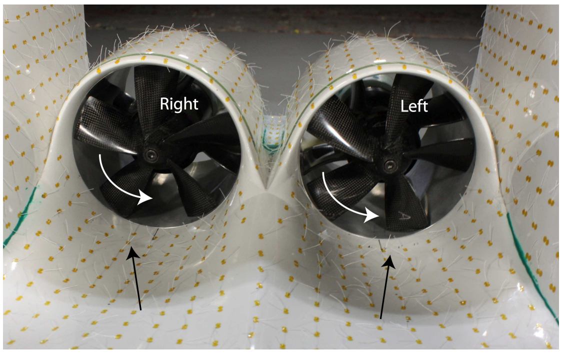

Figure 4.16: Inflow direction and fan rotation

4.4 Mission Points

The important mission points of the D8 aircraft are cruise, start of climb (SOC), top of climb (TOC) and descent. These points are displayed in Figure 4.17 (Hall (2014)), which gives the relation of thrust over drag (T'/D') versus the lift coefficient (C_L). This plot is generated based on the TASOPT-optimized D8.2 configuration. The C_L values correspond to a given angle of attack, given in Table 4.4 for the different configurations, and T'/D' corresponds to a given climb angle, which was used to select the net streamwise force coefficient, (C_X), for the off-design points. A yaw case was added, because aircraft need to be certified for a yaw angle up to 15°. It is chosen to focus on the descent yaw case, because descent, having the lowest value of λ (Equation 4.3) and a high angle of attack, is expected to have the most severe distortion.

To assess the effect of the propulsors on the flow features, use is made of the non-dimensional variable λ, defined by Equation 4.3.

$$\lambda = \frac{\omega \cdot R_{\text{tip}}}{V_\infty} = \frac{U_{\text{tip}}}{V_\infty} \tag{4.3}$$

where ω is the rotational speed, R_{tip} is the rotor radius (equal to 71.8 mm) and V_∞ is the tunnel speed.

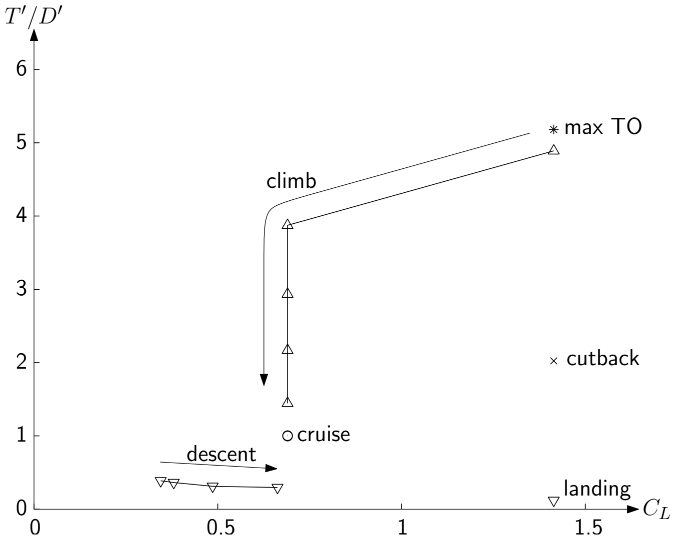

Figure 4.17: Mission points D8, thrust over drag versus lift coefficient at given angle of attack, Hall (2014)

Table 4.4: Important mission points D8

Configuration	α [°]	speed [ms^{-1}]	RPM	λ
Start of Climb	8	18.8	14000	5.6
Top of Climb	2	31.3	14000	3.4
Cruise	2	37.6	13250	2.7
Descent	6	31.3	5250	1.3

Chapter 5

Experimental Set-up

This Chapter describes the set-up of the 1:11 scale D8 wind tunnel model, the mini-tufts flow visualization, and the traverse system for the five-hole probe surveys.

5.1 Wind Tunnel Model

The 1:11-scale D8 wind tunnel model was shipped from MIT (Boston, MA) to NASA (Langley, VA), where it was assembled, Figure 5.1, and then placed in the wind tunnel, Figure 5.2. All connections had to be made to be able to control the propulsors (control the fan wheel speed and measure the electrical power), run the five hole probe traverse, and change the model orientation. The forces and moments are collected by the internal NASA balance.

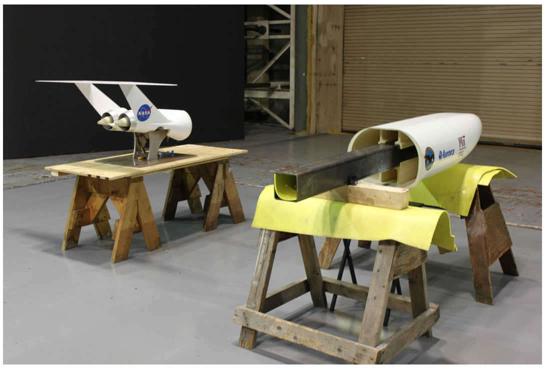

Figure 5.1: 1:11-scale D8 wind tunnel model assembly

Figure 5.2: 1:11-scale D8 wind tunnel model placement

5.2 Mini Tufts

The goal of the mini-tufts is to assess the flow coming into the propulsors. 982 mini-tufts, 20 mm long, were attached to the model in a 20 mm x 20 mm grid, on the fuselage, vertical tails, mini beaver tail and nacelles. The grid can be seen in Figures 5.3 and 5.4. The tufts were attached to the surface by high temperature masking discs (Tape). These discs are not fluorescent and do not leave any residue on the model. Each piece of monofilament thread is attached by two dots, such that the thread is positioned upright, as in Figure 5.5 (attaching it with one dot would result in the thread facing one direction).

Two cameras were used to capture the model from two different views, positioned on top of the wind tunnel looking through a window in the ceiling, as can be seen in Figure 5.6. One camera was positioned above the model and one was focused on the model from the side. The UV-flash was applied from the top of the wind tunnel model at the same time as the picture was taken. The cameras were connected to a laptop, enabling taking and viewing the pictures in the control room.

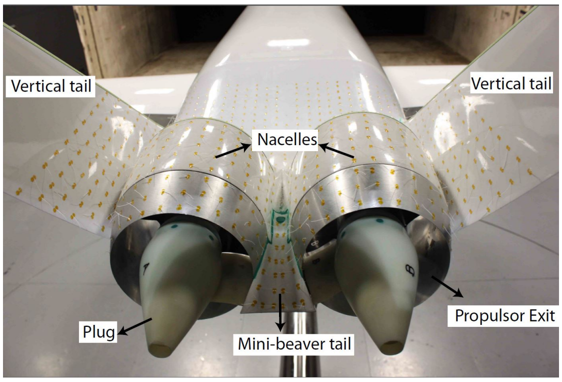

Figure 5.3: Overview mini-tufts, grid, back view

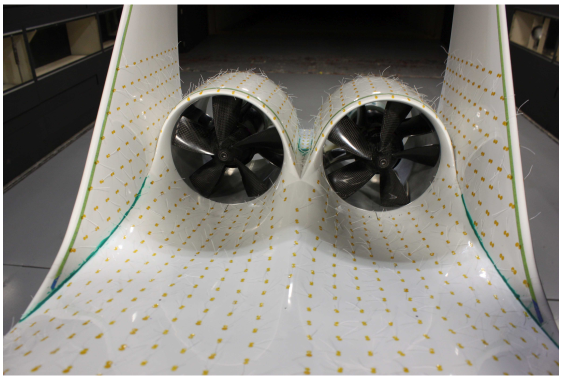

Figure 5.4: Mini-tufts, front view

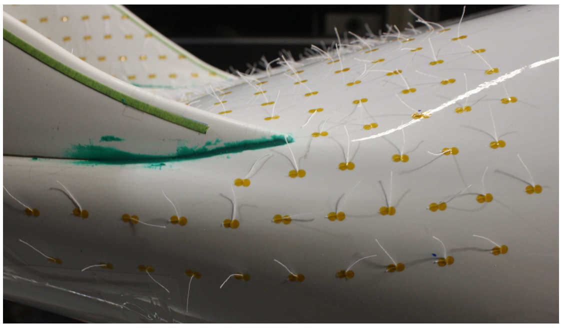

Figure 5.5: Mini-tufts, ‘double dotted’

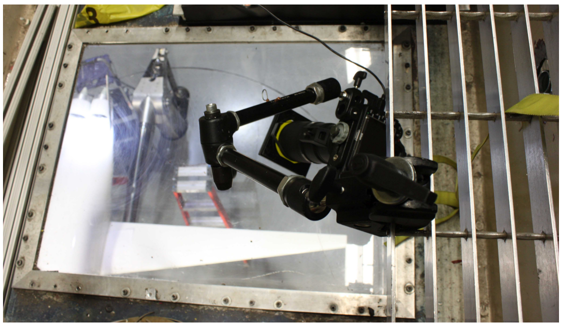

Figure 5.6: Camera position, top wind tunnel, view from side

5.3 Traverse System

The traverse system, described in Section 4.1.5, is set-up using the following procedure:

1. Attach the aluminum vertical bar that connects the traverse system to the model support, Figure 5.8 (number 1).
2. Attach the horizontal arm, a level is used to make sure the arm is horizontal, Figure 5.8 (number 2).
3. Make sure the traverser indexing piece is in place, resting on the screw that attaches the mini beaver tail to the model.
4. Use a string and three pins to make sure the traverse system is aligned, Figure 5.7. One pin is attached to the model and two pins are attached to the traverse system. When tightening the string between the two outer pins, the string should be exactly on the top of the middle pin.
5. Connect the five hole probe and the stepper motor, such that the stepper motors can be controlled from the control room and the pressure values can be read.
6. Run the alignment code, which guides the probe to a number of known points (alignment points). The distance between an alignment point and the actual position of the probe can be measured. Figure 5.9 illustrates the alignment point and Figure 5.10 gives the alignment grid used. The following alignment points are used:
    (a) Mid points of the propulsor
    (b) Reference line on surface, Figure 5.9

The code to control the traverser and guide the five hole probe to the traverse system is described in Appendix B.

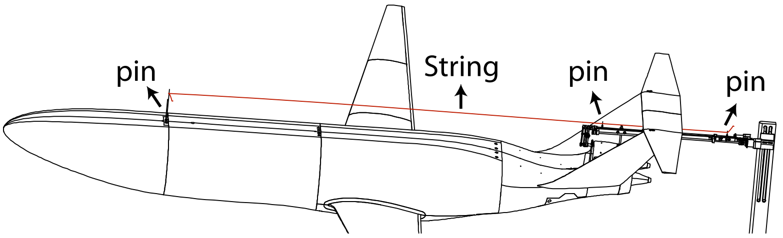

Figure 5.7: Traverse system alignment using a string and three pins

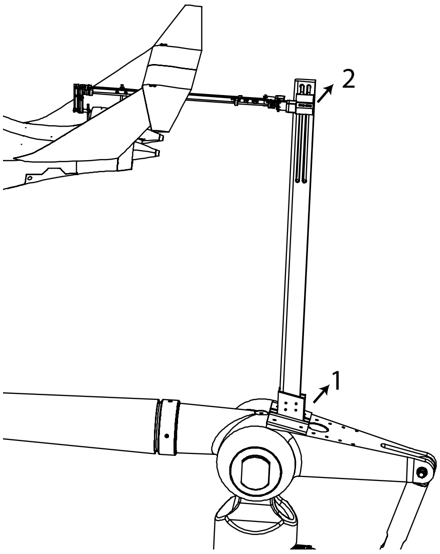

Figure 5.8: Traverse system set-up

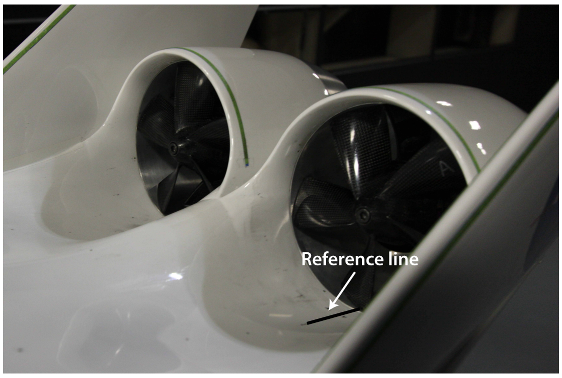

Figure 5.9: Reference line

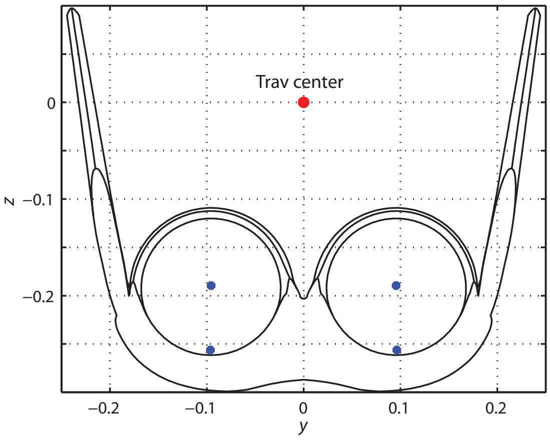

Figure 5.10: Alignment grid

Chapter 6

Results

In this chapter the results are given of the experiments and computations performed to assess the inlet distortions of the D8 at the important mission points, as described in Chapter 4. First the results for each mission point are discussed, which were given in Section 4.4, after which the effect of changing the angle of attack, α, is assessed, and the influence of the model and propulsor on the flow. At the end of this Chapter the values of the power requirement and distortion level found at each mission points for the left and right propulsor are summarized.

6.1 Cruise

Cruise (α=2°, λ=2.7) is the largest part of the flight, and the most important flight condition.

The position of the mini-tufts at cruise is displayed in Figure 6.1. There is no large scale separation seen but there is cross-flow present. There are some blurred tufts at the mini beaver tail, indicating a region of unsteady flow. The flow far from the propulsors is steady, with the tufts all pointing in the flow direction. At the junction of the vertical tail and the fuselage unsteady flow can be seen, with tufts pointing in a random direction, not following the streamline of the D8 body. The overall flow over the nacelles is steady.

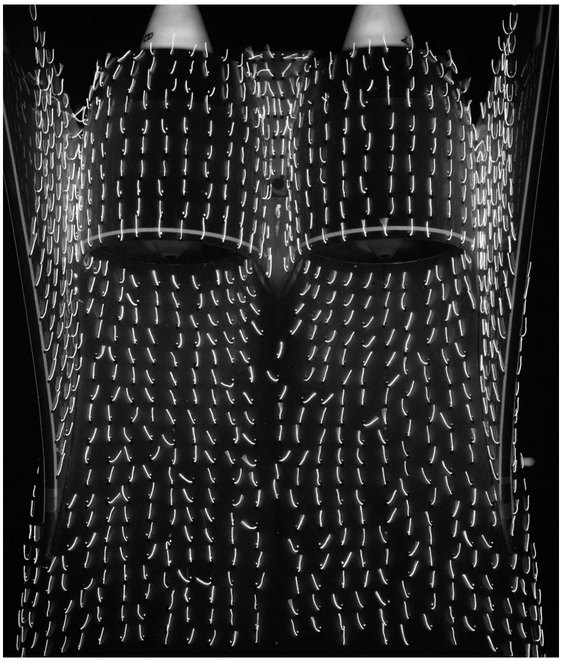

Figure 6.1: Mini-tuft flow visualization, cruise

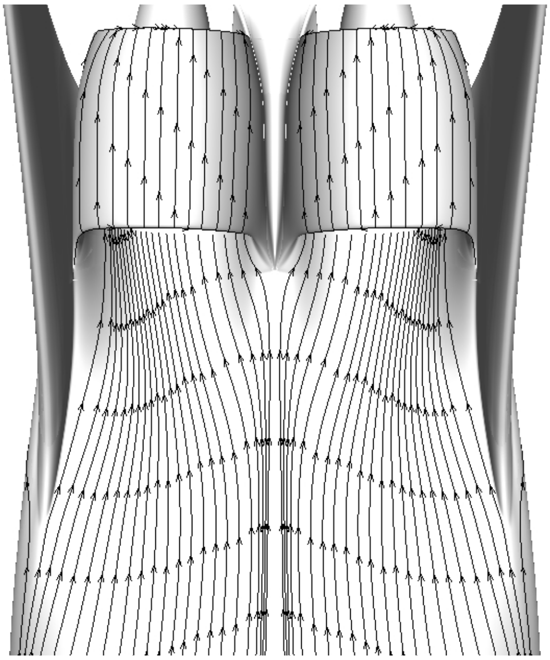

Figure 6.2: Streamlines CFD 0.76 mm above the surface, cruise

Streamlines from CFD were generated at different heights above the surface, as given in Figure C.1, Appendix C. The results for the different heights look similar, analogous to the top of climb condition.

Comparing the streamlines from CFD at 0.76 mm above the surface, Figure 6.2, with the results from the mini-tufts, Figure 6.1, the general trend is similar, there is cross-flow present. No disagreement can be noted. The region of unsteady flow at the junction of the vertical tail with the fuselage indicated by the blurred mini-tufts is smaller than at top of climb, in agreement with the streamlines from CFD. At the top of climb condition the CFD streamlines go around this region, where at the cruise condition the streamlines enter this region.

The result of the five hole probe measurements for cruise is given in Figure 6.3. The measurements were carried out twice. The repeat run was executed several days later, after changing configurations and plugs and is displayed in Figure 6.4.

The vertical pressure stratification shows the presence of the ingested boundary layer. There is an asymmetry between the left and right propulsor, in that the right propulsor has a slightly larger region of low pressure (dark blue) on the bottom of the propulsor. This is caused by cross-flow, which can be seen in the streamlines in Figure 6.2. The asymmetry is more distinct than at the top of climb condition and is confirmed by a higher difference in DC(60) and C_{P_S} between the left and right propulsor, illustrated in Table 6.1. The values of DC(60) for both runs lie within 1% of each other, confirming the repeatability of the measurements. The settling time of the probe was long enough, the traverse system was reassembled correctly, and the tunnel conditions did not change or were not of influence.

Table 6.1: DC(60) and C_{P_S}, cruise (experiments)

	run	DC(60)	C_{P_S}
Left	1	0.32	0.015
	2	0.32	
Right	1	0.37	0.016
	2	0.36	

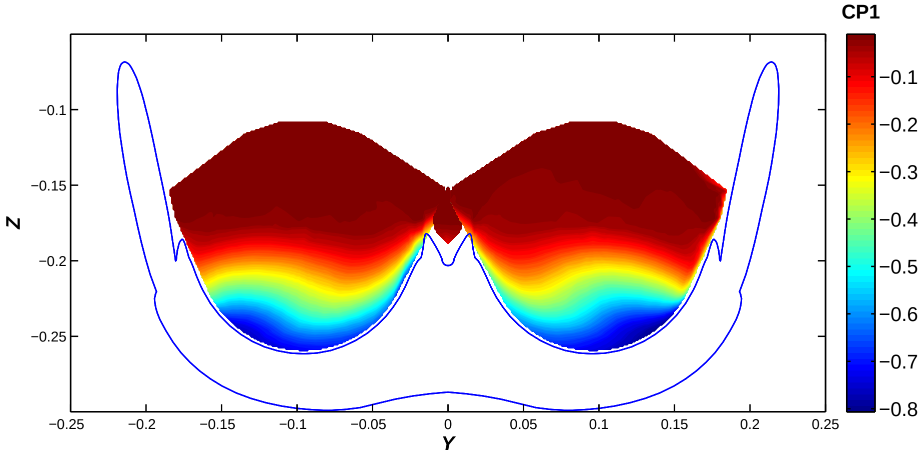

Figure 6.3: Five hole probe survey inlet, cruise (α=2°, λ=2.7), C_{P_1}

The pressure distribution from the five hole probe measurements, Figure 6.3 is compared to the pressure distribution from CFD, Figure 6.5. The asymmetry observed from the probe survey cannot be noted, because the CFD only assessed the right side of the model. The general trend for the pressure coefficients is the same, the pressure coefficients are in the same range, there is a vertical pressure stratification, and the lowest pressure coefficients concentrate on the bottom of the propulsors, biased to the sides due to the cross-flow. DC(60) from CFD is 0.30, compared to 0.34 from the five hole probe measurements, which is within 6% of each other. The worst 60° sector found by CFD was between -97.6°and -37.6°, and for the five hole probe between -104.6°and -44.6°(right propulsor), as in Figure 6.6. This confirms the good agreement between CFD and experiments.

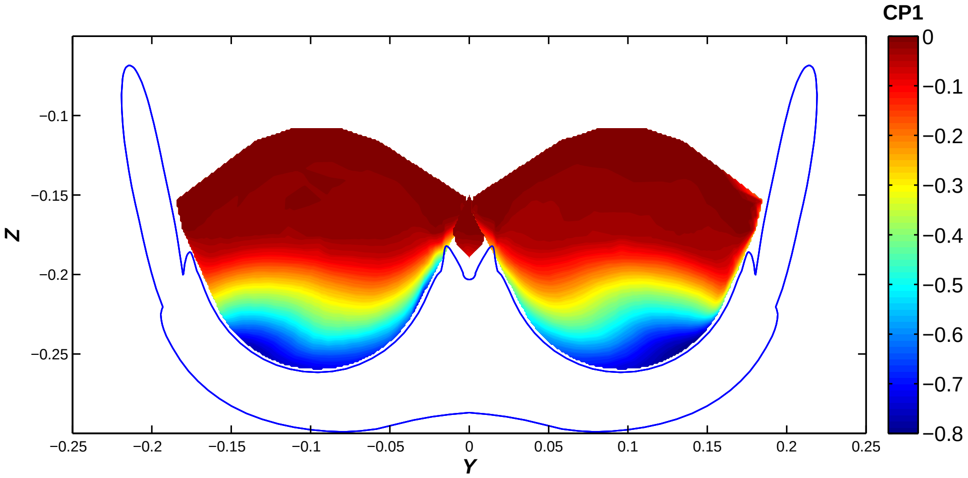

Figure 6.4: Five hole probe survey inlet, cruise (α=2°, λ=2.7), C_{P_1}, repeat run

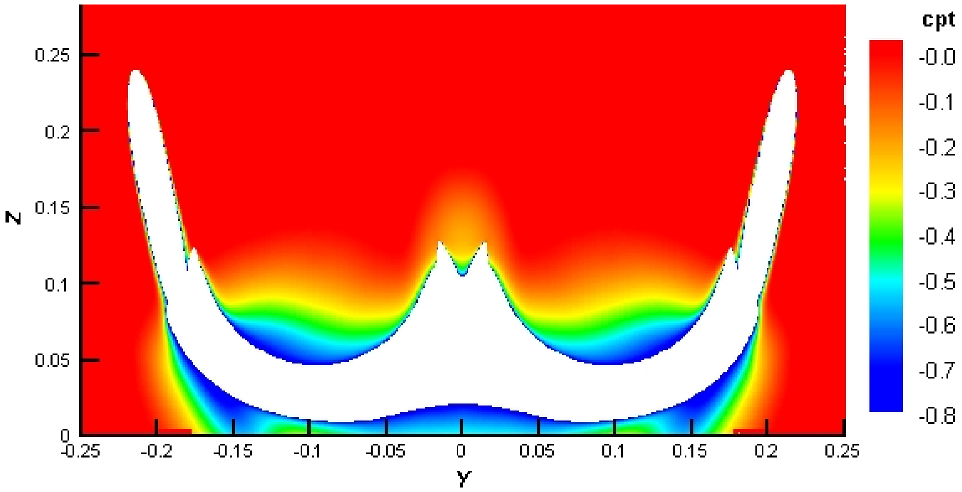

Figure 6.5: CFD calculations at plane of five hole probe measurements, C_{P_t}, cruise

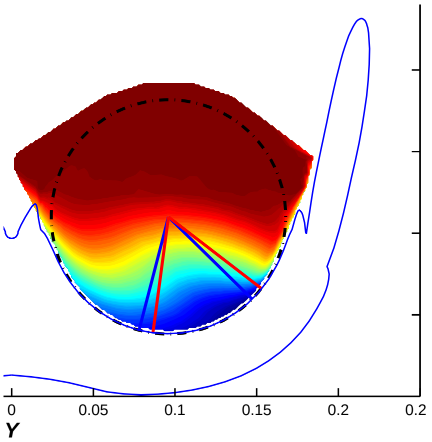

Figure 6.6: Worst 60° sector from CFD (red) and FHP (blue), right propulsor, cruise

6.2 Start of Climb

Figure 6.7 shows the mini-tufts at start of climb (α=8°, λ=5.6). There is strong cross-flow into the propulsors. At the junction of the vertical tail and the fuselage some unsteady flow can be noted, which could have come from the sides of the model. The overall flow over the nacelles is steady. The start of climb condition has the highest α of all conditions examined (8°), however the flow features look similar to the top of climb condition (α=2°, Figure 6.9), indicating a small influence of α on surface streamlines. The flow at the mini-beaver tail, the area between the propulsor exits, is outside of the camera view due to high α.

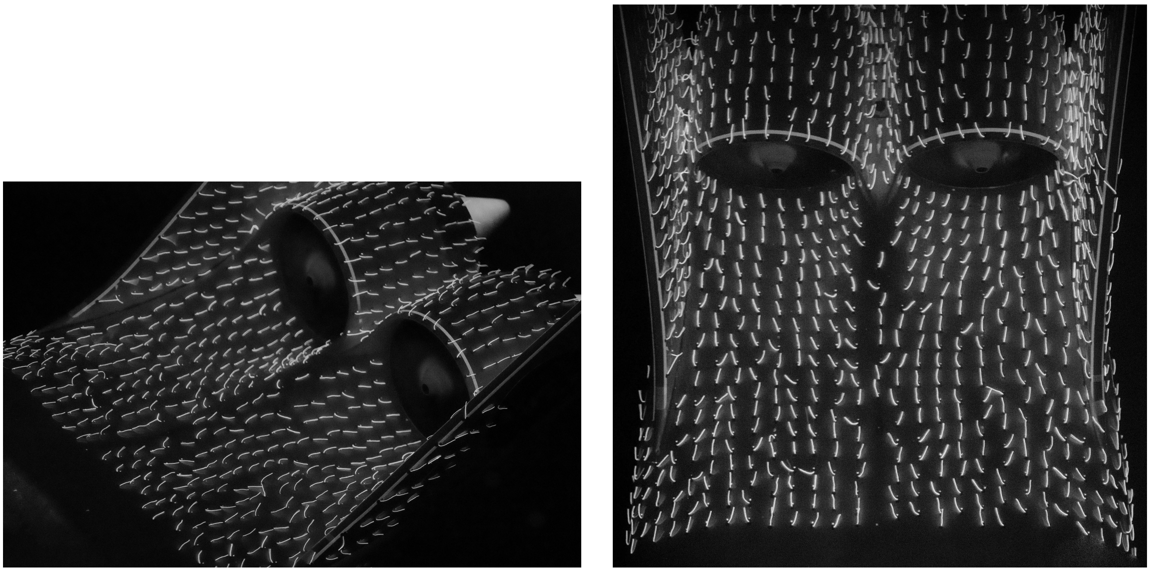

Figure 6.7: Mini-tufts flow visualization, start of climb (λ=5.6, α=8°)

The result of the five hole probe survey at start of climb in terms of C_{P_1} is given in Figure 6.8. Comparing Figure 6.8 to cruise, Figure 6.3, the main difference is the absence of the stratified pressure distribution, indicating the ingested boundary layer at top of climb. Engine suction, due to the high value of λ, makes the distortion less severe.

The value of C_{P_1} on the top side of the propulsor is not equal to zero, as is the case for the top of climb condition, indicating that there is no free-stream flow ingested at this condition.

The flow close to the propulsor nacelles has separated, indicated by the low pressure values (dark blue).

The pressure distribution is slightly asymmetric, which is caused by cross flow at the model fuselage. This is confirmed by the difference in power requirement and distortion coefficient between the left and right propulsor. The right propulsor has a higher distortion coefficient and power requirement (DC(60)=0.11), C_{P_S}=0.017) than the left propulsor (DC(60) = 0.096, C_{P_S}=0.015). The low value of DC(60) for both propulsors can be explained by the definition of DC(60), as it is a localized distortion descriptor.

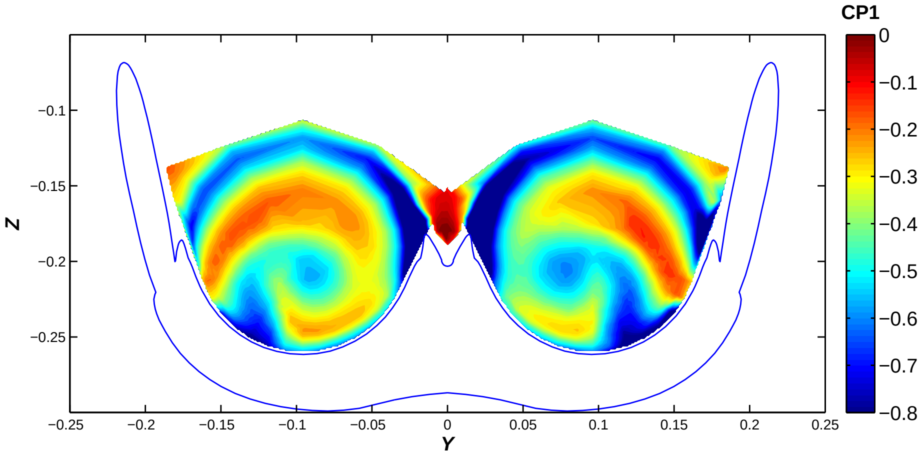

Figure 6.8: Five hole probe survey inlet, start of climb (α=8°, λ=5.6), C_{P_1}

6.3 Top of Climb

A top view of the tufts at top of climb (α=2°, λ=3.4) is given in Figure 6.9, once again, there is cross-flow into the propulsors. This is comparable to the start of climb condition. However, there is no unsteady flow at the junction of the vertical tail and the fuselage, the overall flow over the nacelles is steady. Close to the mini beaver tail there are a few blurred tufts, indicating unsteady flow.

It is not known at what height the mini-tufts capture the flow, therefore streamlines from CFD were generated at different heights above the surface, as in Appendix C, Figure C.2. The results look similar for the heights assessed, so the mini-tufts are compared to CFD at 0.76 mm from the surface, Figure 6.10. The general trend between the experiments and CFD is similar, there is cross-flow present. The mini-tufts indicate a region of blurred tufts flow near the junction of the vertical tail and fuselage. The streamlines from CFD, which were generated at equal distance from each other upstream of the leading edge of the vertical tail, are directed around this region, indicating blockage and lower velocity flow. It is possible that the vertical flow present in this region is unsteady.

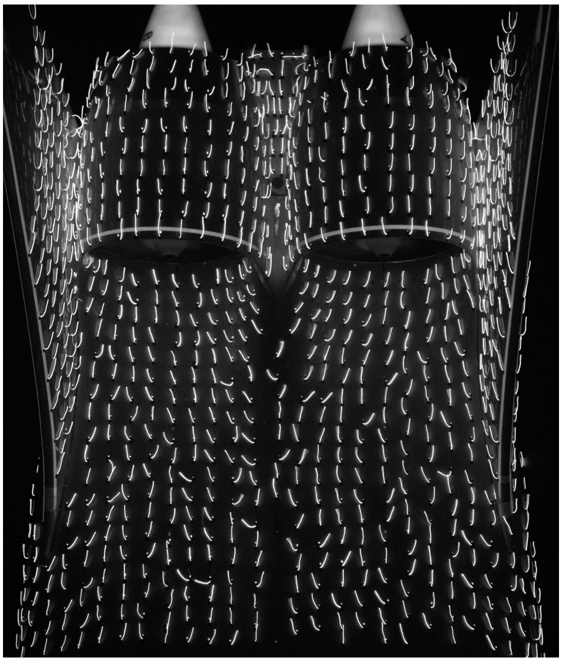

Figure 6.9: Mini-tuft flow visualization, top of climb

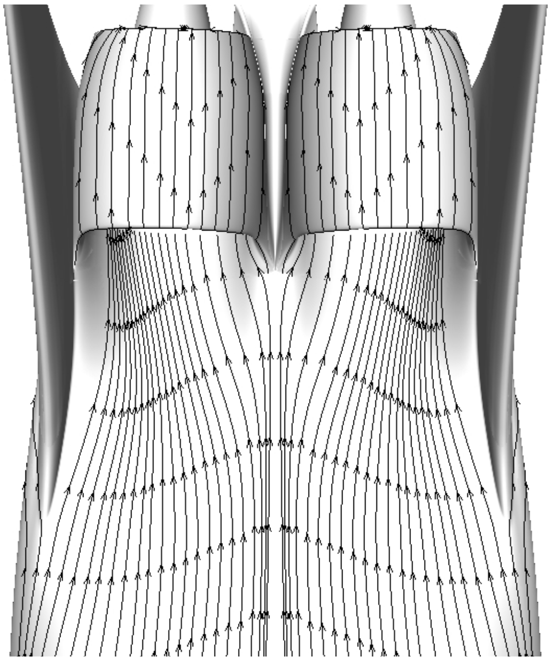

Figure 6.10: Streamlines CFD 0.76 mm above the surface, top of climb

The result from the five hole probe survey at top of climb is given in Figure 6.11. The ingested boundary layer can be seen by the stagnation pressure stratification at the lower part of the propulsor face. The lowest pressure coefficients concentrate near the sides of the propulsors close to the vertical tail, due to cross flow, as in Figure 6.10. There is a small difference in DC(60) and C_{P_S} between the left (DC(60)=0.30, C_{P_S}=0.015) and right propulsor (DC(60)=0.32, C_{P_S}=0.16). The distortion is higher than at the start of climb condition, because the distortion concentrates on the bottom of the propulsor, resulting in higher maximum pressure differences at the inlet.

The results from the five hole pressure measurement, Figure 6.11 are compared to the results from CFD, Figure 6.12. The color-bar of the plots is set such that the same colors represent the same pressure coefficient values in both figures. The pressure distribution looks similar and has similar pressure coefficient values. DC(60) from CFD equals 0.32, compared to the average value of 0.31 found from the five hole probe surveys, which is within 1% of each other. The worst 60° sector found by CFD was between -97.6°and -37.6°, and for the five hole probe between -106.4°and -46.4°(right propulsor), illustrated in Figure 6.13.

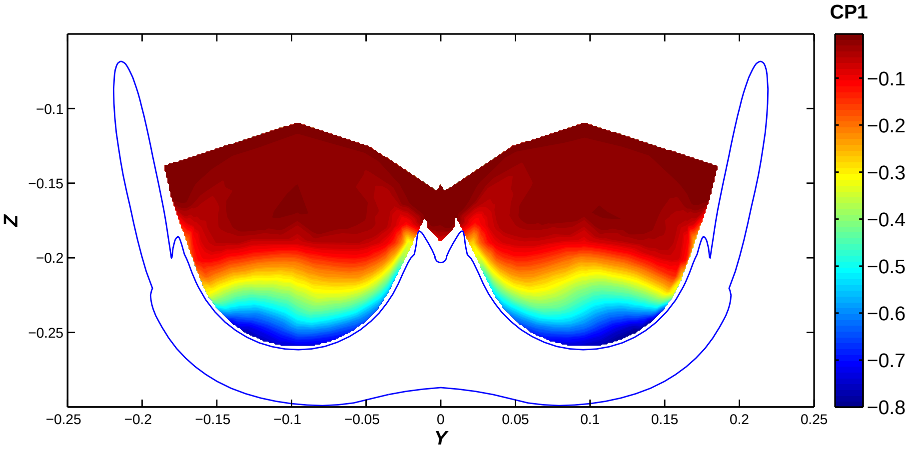

Figure 6.11: FHP survey inlet, top of climb (α=2°, λ=3.4), C_{P_1}

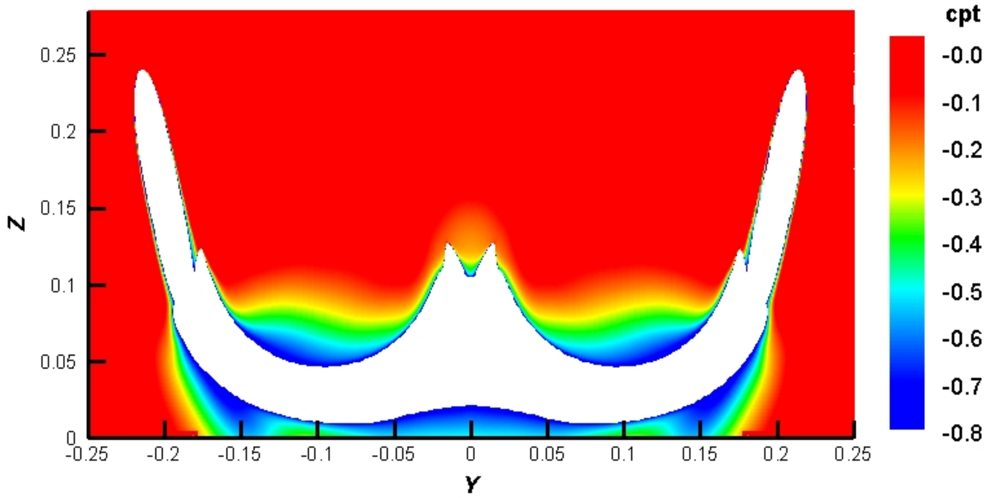

Figure 6.12: CFD at plane FHP measurements, top of climb (α=2°, λ=3.4), C_{P_t}

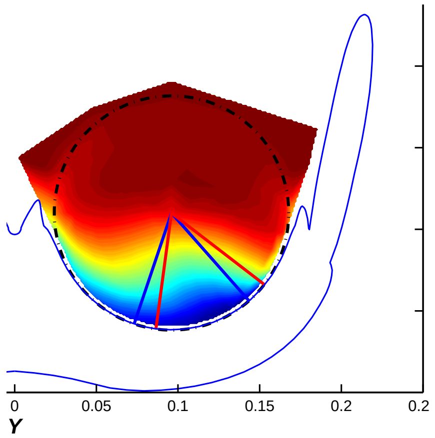

Figure 6.13: Worst 60° sector CFD (red) and FHP (blue), right propulsor, top of climb

6.4 Descent

The descent condition (α=6°, λ=1.3) has the lowest value of λ of all mission points and a high α and is therefore expected to have the most severe inlet distortions.

Figure 6.14 displays the results of the mini-tuft flow visualization at the descent condition. A large region of blurred tufts indicate unsteady flow starting near the leading edge of the vertical tail and continuing inwards and towards the propulsor inlet. The region of unsteady flow is larger than at for all other mission points. The cross-flow is more severe than at any of the other conditions considered and can also be seen in the result from mini-tuft flow visualization from entry 1, Figure 6.15. Longer tufts of different material made the flow angle more distinct.

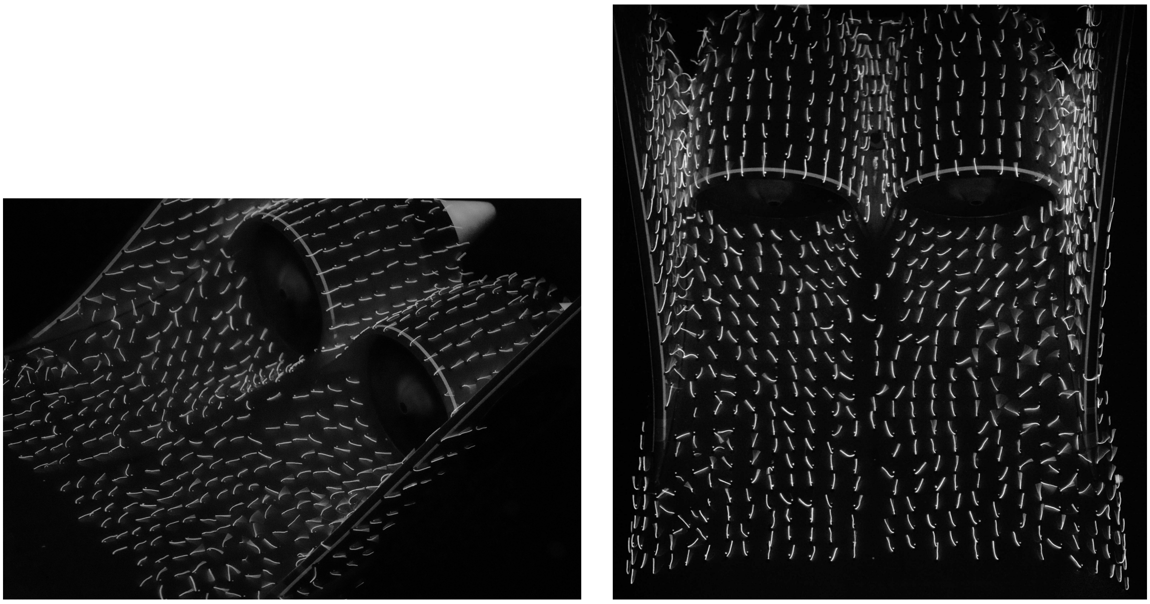

Figure 6.14: Mini-tufts flow visualization, descent (λ=1.3, α=6°)

The five hole probe measurements are given in Figure 6.16. A vortex is entering both engines from the top/side. The forming of this vortex can be seen in the picture of the mini-tufts from the side, Figure 6.14, at the junction of the vertical tail and the fuselage. The asymmetry noted with the mini-tufts can be seen in the pressure distribution and is confirmed by a 46% difference in C_{P_S} between the left and right propulsor, compared to 4-10% for the other conditions, and by a 32% difference in DC(60), compared to 4-12% for the other condition, Table 6.3. The right propulsor has a DC(60) of 0.33, the left of 0.24. The region of low pressure at the outer top part of the propulsor is outside the capture area of the propulsor and is not included to calculate DC(60).

Increasing α to 8° results in a lower DC(60) (left: 0.16, right: 0.23), because the lowest pressures are now outside the radius of capture of the propulsor. The influence of α is further assessed in Section 6.6.

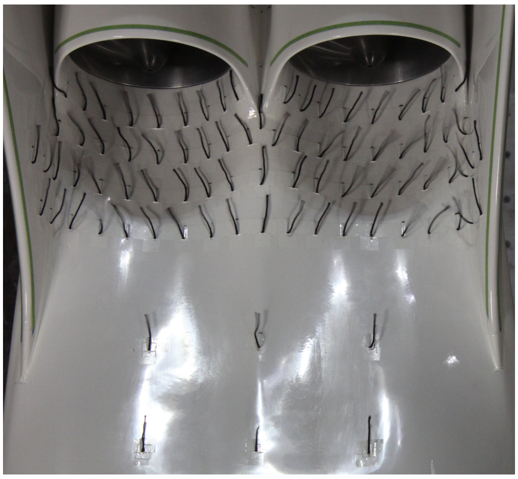

Figure 6.15: Mini-tufts flow visualization, descent (α=6°, λ=1.3), entry 1

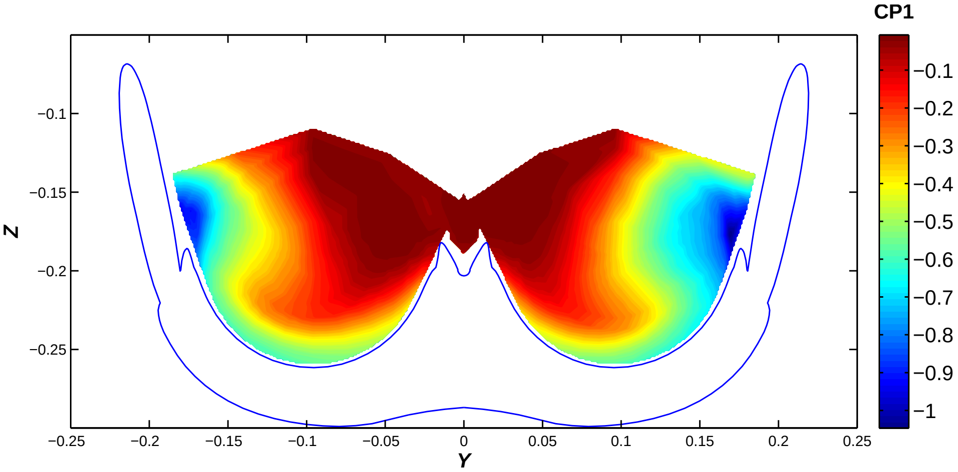

Figure 6.16: Five hole probe survey inlet, descent at $6°$, λ=1.3, C_{P_1}

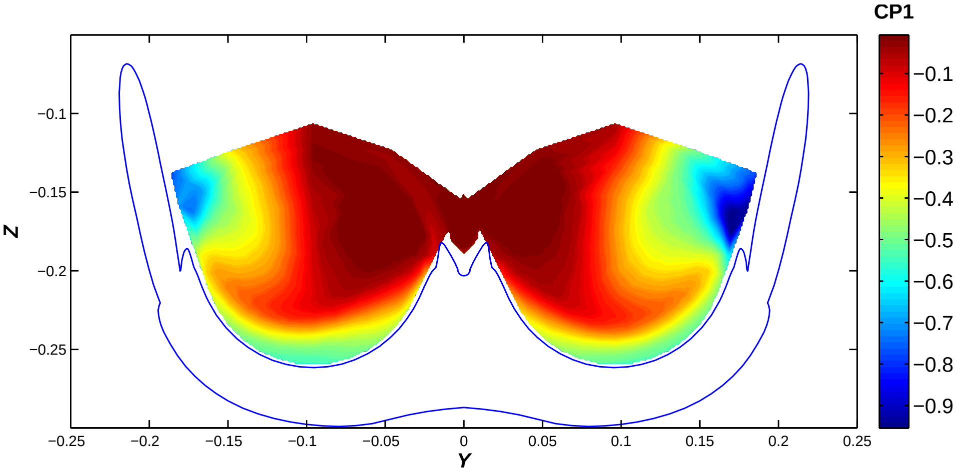

Figure 6.17: Five hole probe survey inlet, descent at $8°$, λ=1.3, C_{P_1}

6.5 Descent, ±15° Yaw

The descent condition is the condition with the highest level of distortions because of the low value of λ and the high value of α and performing a yaw maneuver at this condition will result in the most severe distortions.

The results from the mini-tufts flow visualization at β=-15° during descent is given in Figure 6.18, and for β=+15° in Figure 6.19. The results are similar, so only β=-15° is discussed. Several regions of unsteady flow can be identified. The region in front of the right engine entirely consists of blurred tufts, indicating unsteady or separated flow. Cross-flow is present, and the inflow angle for the left engine is larger than for any of the assessed conditions, see Table 6.3. The inflow angle for the right propulsor cannot be determined because of the blurred tufts. Flow from the sides of the fuselage and from the leading edge of the nacelles is going towards the propulsor and flow is going over the top of the vertical tail.

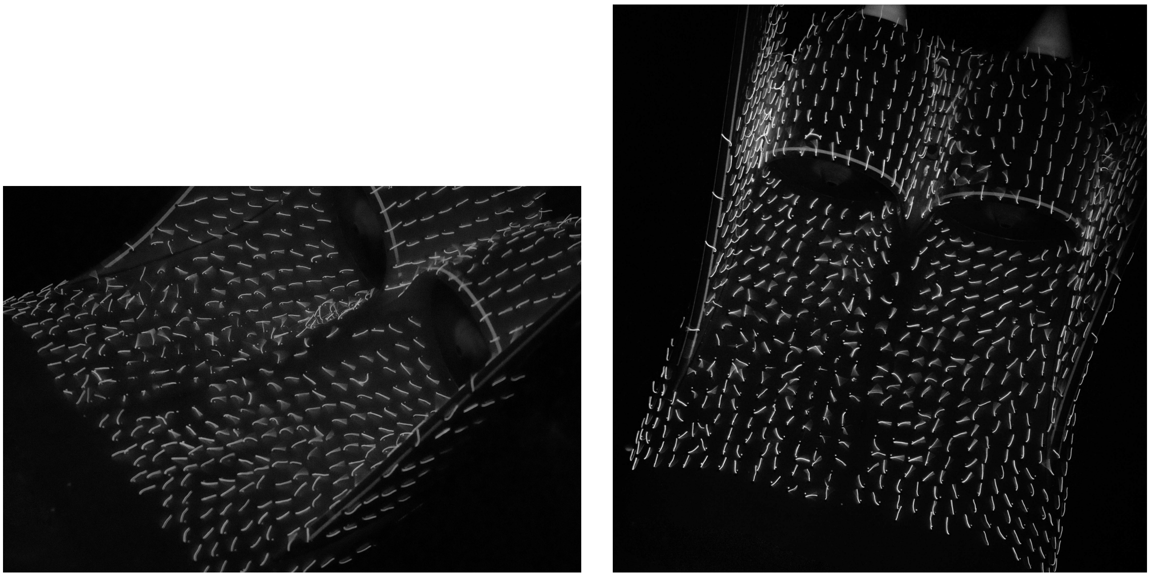

Figure 6.18: Mini-tufts flow visualization, descent, α=6°, λ=1.4, -15° yaw

The five hole probe measurements at $\beta\pm15°$ are given in Figures 6.20 and 6.21, only the results for +15° are discussed. The region of low pressure at the right propulsor corresponds to a region with high cross flow, as in the results from the mini-tufts. The left engine has a larger region of low pressure (light blue), however the value of the pressure is not as low as is the case at the right engine (dark blue). The larger light blue area at the right propulsor corresponds to the ingestion of separated flow, indicated by the blurred tufts in front of the right propulsor in Figure 6.19. Both regions of lower pressure are located more towards the outer side of the propulsors, suggesting that a vortex is generated at the junction of the vertical tail and the fuselage. At the right propulsor, a region of lower pressure near the mid/top part of the propulsor can be

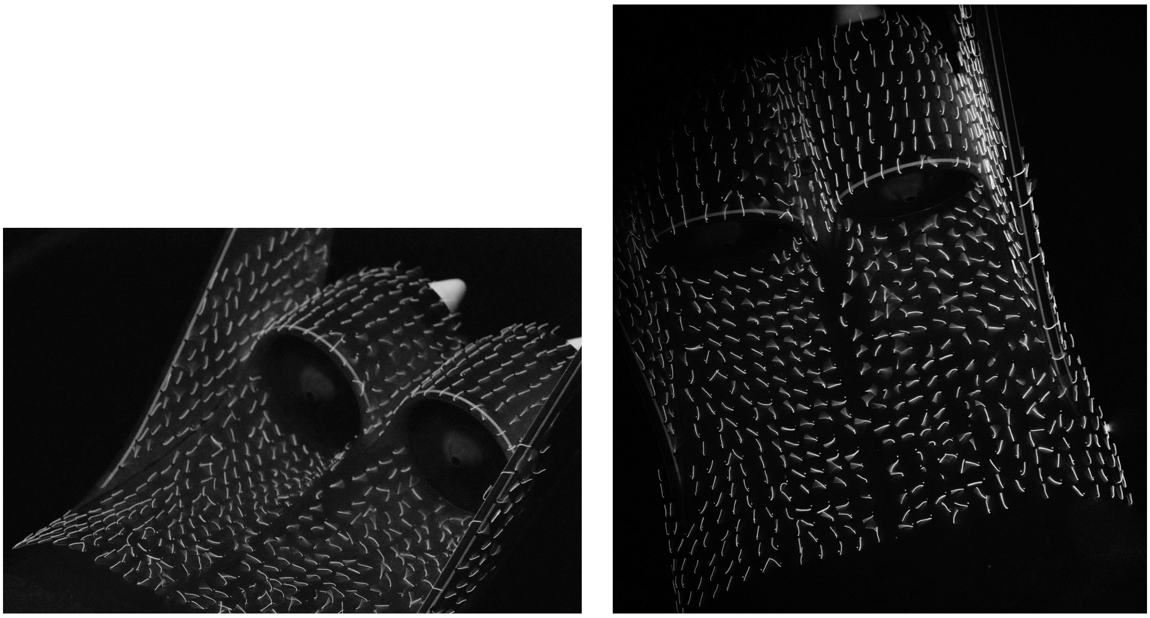

Figure 6.19: Mini-tufts flow visualization, descent, α=6°, λ=1.3, +15° yaw

noted, corresponding to a region of blurred tufts on the nacelle of the right propulsor.

The left engine has a distortion coefficient of 0.31 (β=+15°) and 0.51 (β=-15°). The right engine has a distortion coefficient of 0.55 (β=+15°) and 0.30 (β=-15°). The difference in DC(60) between the left and right propulsor is around 50%.

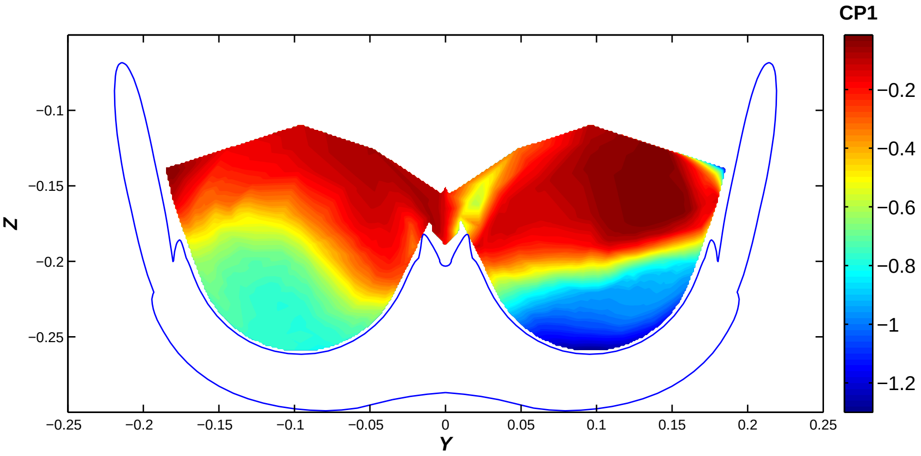

Figure 6.20: Five hole probe survey inlet, descent, yaw (β=+15°), C_{P_1}

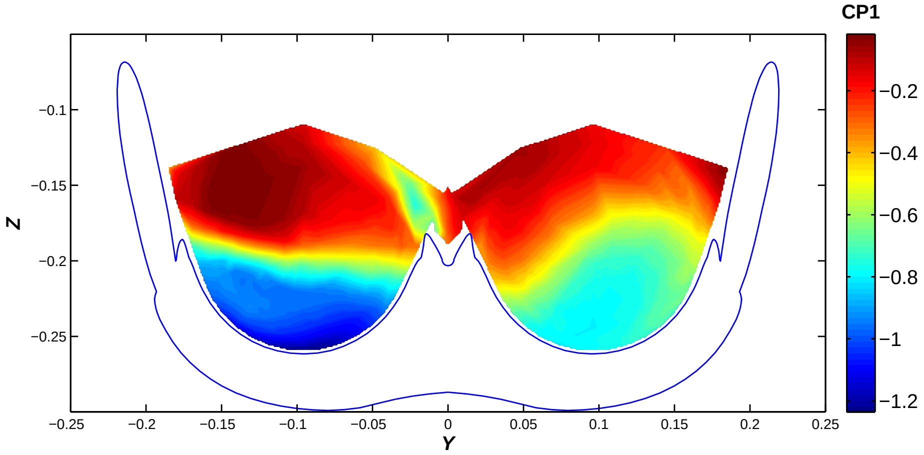

Figure 6.21: Five hole probe survey inlet, descent, yaw (β=-15°), C_{P_1}

6.6 Effect of Angle of Attack

The effect of α on the inlet distortions was studied by mini-tuft flow visualization and five hole probe surveys at various α keeping λ constant at 3.4. The mini-tufts were assessed at α=2°, 4°, 6° and 8° for λ=3.4, and the result is given in Appendix D, Figures D.1, D, D.2, and D.3. The influence of α on the streamlines is barely notable.

The result from five hole probe surveys at α=2°, 6° and 8° for λ=2.7 (31.3 ms^{-1}, RPM=11100) is given in Figures 6.6, 6.22, and 6.23. At α=2°, the flow looks similar to the top of climb and cruise condition and the ingested boundary layer can be noted clearly. At α=6° the pressure distribution changes significantly, the ingested boundary layer is barely notable and a vortex is formed coming in from the side. At α=8° this vortex is shifted up, entering the propulsors higher.

DC(60) calculated from the pressure surveys decreases with increasing α, as can be seen in Table 6.2, as the low stagnation pressure flow is out of the propulsor capture area, and the distortion is spread over the propulsor inlet.

Table 6.2: Distortion coefficient DC(60) for increasing α, at λ=2.7

α	DC(60)	
	left	right
2°	0.321	0.364
6°	0.299	0.327
8°	0.225	0.254

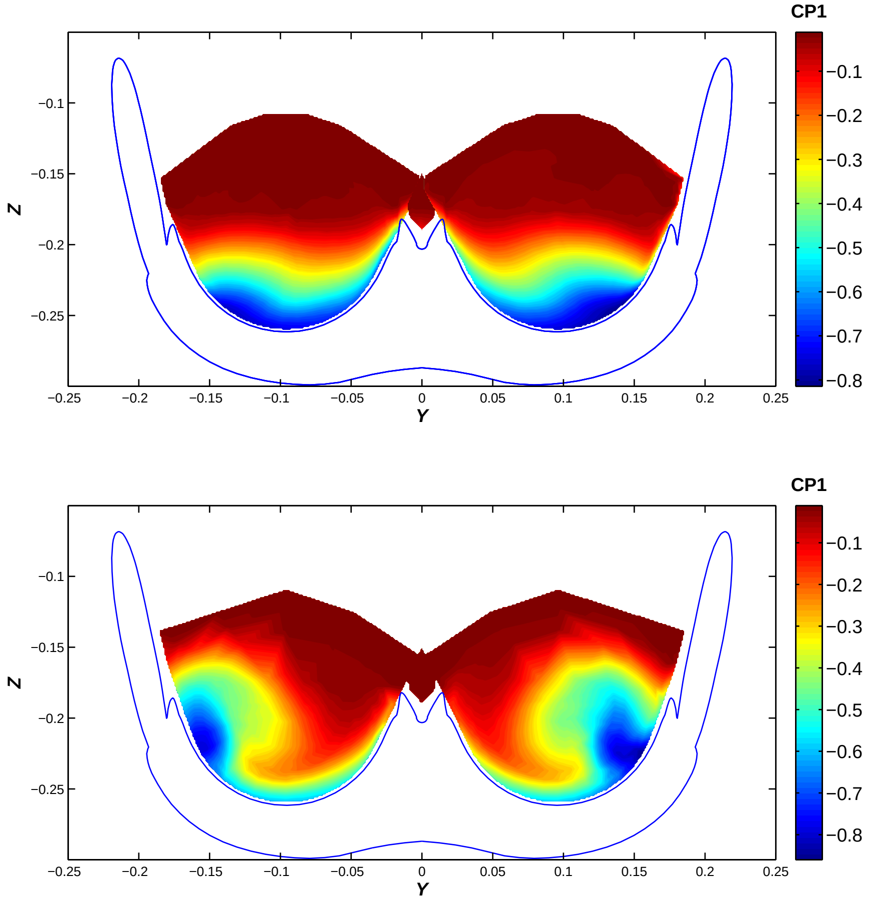

Figure 6.22: Five hole probe survey, α-effect, α=2°(top), 6°(bottom), λ=2.7, C_{P_1}

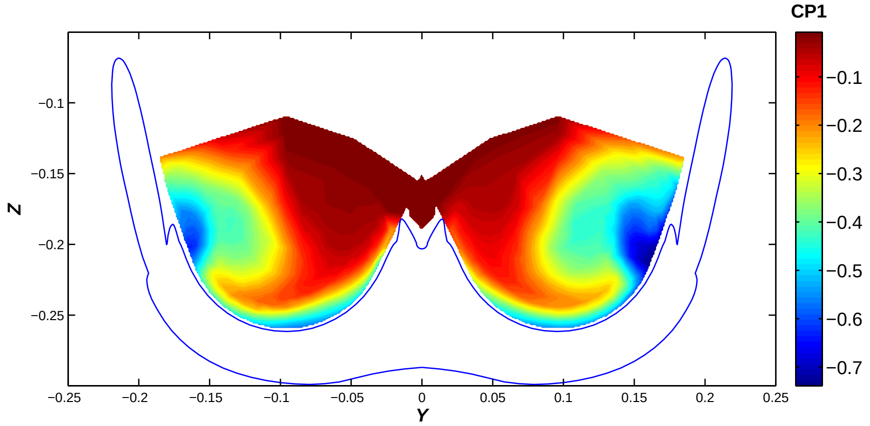

Figure 6.23: Five hole probe survey, α-effect, α=8°, λ=2.7, C_{P_1}

6.7 Summary of the Results at the D8 Mission Points

Table 6.3 gives a summary of the power requirement, C_{P_S}, distortion coefficient, DC(60), and inflow angle for each condition, and the difference between the left and right propulsor. The inflow angle is measured using the convention given in Figure 6.24. It is assumed that a change in α from 2° to 8° does not influence the flow angle measured in the pictures, because the angles are small and the camera is positioned approximately two meters above the wind tunnel model, compared to a tuft length of 19 mm.

The lowest value of DC(60) is 0.11 at the start of climb condition. This condition has the highest value of λ, and no vertical pressure stratification can be noted in the plot of the pressure distribution from the five hole probe surveys. The top of climb and cruise condition have a lower value of λ, and a clear vertical pressure stratification at the propulsor bottom.

The difference in DC(60) and C_{P_S} between the left and right propulsor is caused by cross-flow from the model surface in combination with the rotation direction of the fan. The right propulsor has the inflow opposite to the direction of rotation of the fan, resulting in a higher power requirement and distortion coefficient for all conditions. At lower values of λ the influence of the propulsors is less, resulting in a higher difference in C_{P_S} and DC(60). Increasing α increases the cross flow. Therefore the top of climb condition (low α and high λ) has the lowest difference in C_{P_S} and DC(60) of all conditions considered.

Yawing the model results in large regions of separation. The flow in front of one propulsor is completely separated and the other propulsor experiences large inflow angles of up to 70%, resulting in a difference of up to 50% in DC(60) between the propulsors.

For the top of climb and cruise condition CFD data was available. The values of DC(60) from CFD and from experiments are within 1% for top of climb and within 6% for cruise.

Table 6.3: Difference in C_{P_S}, DC(60) and flow angle for the left and right propulsor

Config	α	λ	C_{P_S}			Flow angle		DC(60)			
			L	R	Δ	L	R	L	R	Δ	CFD
SOC	8°	5.6	0.0151	0.0167	10%	15°	-10°	0.096	0.108	12%	-
TOC	2°	3.4	0.0153	0.0160	4.0%	10°	-10°	0.299	0.317	5.8%	0.315
Cruise	2°	2.7	0.0148	0.0158	6.2%	15°	-10°	0.323 0.320	0.365 0.364	12% 13%	0.303
Descent	6°	1.3	0.0089	0.0143	46%	40°	-30°	0.238	0.329	32%	-
15° yaw	6°	1.3	-	-	-	-	-65°	0.311	0.551	46%	-
-15° yaw	6°	1.4	-	-	-	70°	-	0.406	0.295	53%	-

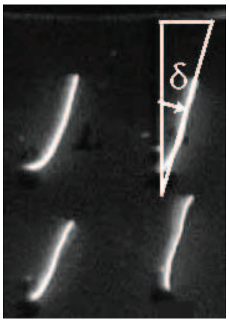

Figure 6.24: Flow angle convention

Chapter 7

Conclusions

- Boundary layer ingestion (BLI), ingesting the fuselage and/or wing boundary layer in the propulsion system, results in a non-uniform pressure distribution at the fan-face, leading to higher inlet total pressure distortions, compared to a non-BLI configuration. The pressure distortion is assessed by the distortion coefficient, DC(60), the maximum variation in pressure over a specified circumferential segment (60°). Conventional (non-BLI) aircraft have DC(60)$\sim$0.1-0.2. The D8 (BLI) aircraft has DC(60)$\sim$0.3 at cruise, determined from experiments and computations.
- The distortion is dependent on:
  - *Model / aircraft configuration.* The main influence of the airframe on the distortions for the D8 configuration is the generation of cross-flow, the flow is directed to the sides of the model when entering the propulsors. Both fans rotate in the same direction, the inflow to the right propulsor is opposite to the rotation direction of the fan, and the inflow to the left propulsor is in the direction of the fan rotation. The right motor therefore has a higher power requirement and a higher DC(60). The difference in DC(60) and power requirement is between 5-50%, dependent on the flight condition.
  - *Flight condition*, defined by α, the angle of attack, λ, the ratio of tip velocity over tunnel speed, and β, the yaw angle.
    The influence of λ is strongest, increasing λ lowers the distortion. At a high value of λ the pressure differences at the fan-face are reduced, lowering the distortions and counter-acting the cross-flow. A low value of λ means a relative lower influence of the propulsor on the flow, such that the propuslor is not able to (fully) counter-act the cross-flow, resulting in a higher difference in DC(60) and power required between the left and right propulsor.
    Changing α increases the cross-flow and changes the location of the regions of

lower pressure, which in some cases lowers the distortion coefficient, because it affects the overall average pressure, and some distortions will be outside of the radius of capture of the propulsor.

Yawing the propulsor results in large regions of separation, the engine is in this case an obstruction in the flow, as it is not aligned with the inflow direction. A combination of a large yaw angle β, a low value of λ, and a high value of α will result in the most distortions.

- There are no areas of high loss/separation for the D8 aircraft that were not anticipated. Most importantly, at cruise the incoming flow is well behaved.
- The mission points assessed for the D8 were start of climb ($\alpha = 8°$, λ=5.6), top of climb ($\alpha = 2°$, λ=3.4), cruise ($\alpha = 2°$, λ=2.7) and descent ($\alpha = 6°$, λ=1.3). The top of climb condition (low α, high λ) has the lowest difference in power requirement and DC(60) of all conditions considered. The start of climb condition (highest λ) has the lowest DC(60). Descent (lowest λ, high α) has the highest difference between the left and right propulsor.
- Changing the flight condition directly influences the pressure distribution at the fan-face. The streamlines only change for a low value of λ in combination with a high value of α and/or β.
- The results from experiments agree well with CFD, there is a 1% deviation in DC(60) at top of climb condition, and 6% at cruise. The pressure distributions look similar, and the pressure coefficient values are roughly equal. The CFD used an actuator disc model to model the propulsors, which does not take into account fan rotation. The result from CFD is therefore symmetrical, and the difference between CFD and experiments is related to the degree of asymmetry in the experiments. The cruise condition has a lower value of λ and more asymmetry than the top of climb condition, resulting in a higher deviation between the CFD and experiments.
- Good collaboration MIT, NASA, Pratt&Whitney, and Aurora Flight Sciences.

Chapter 8

Recommendations

- The inlet pressure distortions are assessed by the distortion coefficient, DC(60), the maximum variation in pressure over a specified circumferential segment of 60°. A lower DC(60) does not always mean a low distortion level. If the distortions are more spread, the average total pressure changes, lowering the maximum variation in pressure, and if the distortions are located towards the propulsor mid, these will not be included in a 60° sector. Different methods/distortion coefficients should be considered to assess the distortion.
- Conventional (non-BLI) aircraft have DC(60)$\sim$0.1-0.2. The D8 (BLI) aircraft has DC(60)$\sim$0.3 at cruise. Research has to be performed to determine the fan response (aerodynamic and aeromechanic) to these higher distortion levels and the impact on the engine life.
- The influence of the higher distortions and power requirement for the right propulsor on the performance of the aircraft, the difference in engine life between the propulsors, and maintenance requirements should be investigated.
- The D8 aircraft uses conventional engines, which are optimized for a uniform inflow. Developing BLI-optimized engines will increase the BLI benefit.
- The D8 model caused cross-flow, resulting in a difference in power and distortion coefficient between the left and right propulsor. The configuration can be optimized to reduce or eliminate this cross-flow. The use of counter rotating fans could be further investigated.
- CFD calculations were performed for two mission points, top of climb and cruise. To further assess the quality of the CFD results, simulations for the start of climb and descent conditions should be performed and compared to the experiments.

Bibliography

Aero-naut. Aero-naut. URL http://www.aero-naut.de/. visited on 2015-01-28.

AeroProbe Corporation. Product Abstract. URL http://www.aeroprobe.com/uploads/Conventional.pdf. visited on 2015-01-02.

Ametek Programmable Power. Sorensen. URL http://www.programmablepower.com/brands/sorensen.htm. visited on 2015-01-28.

S.W. Ashcraft, A.S. Padron, K.A. Pascioni, G.W. Stout, and D.L. Huff. Review of Propulsion Technologies for N+3 Subsonic Vehicle Concepts. Technical Report NASA\TM-2011-217239, National Aeronautics and Space Administration (NASA), October 2011.

O. Atinault, G. Carrier, R. Grenon, C. Verbecke, and P. Viscat. Numerical and Experimental Aerodynamic Investigations of Boundary Layer Ingestion for Improving Propulsion Efficiency of Future Air Transport. *AIAA 2013-2406*, June 2013.

J.B. Barlow, W.H. Rae, and A. Pope. *Low-speed wind tunnel testing*. ISBN: 0471557749. Wiley, New York, USA, 3rd edition, 1999.

S.M. Boller. One-dimensional dynamic wake response in an isolated rotor due to inlet total pressure distortion. Master's thesis, Virginia Polytechnic Institute and State University, October 1998.

P.G. Buning. Pieter G. Buning's Home Page. URL http://aaac.larc.nasa.gov/~buning/. visited on 2014-03-25.

W.M. Chan, S.E. Rogers, S.A. Pandya, D.L. Kao, and P.G. Buning. Chimera Grid Tools User's Manual. URL http://people.nas.nasa.gov/~wchan/cgt/doc/man.html. visited on 2015-01-20.

D.L. Daggett, R. Kawai, and D. Friedman. Blended Wing Body Systems Studies: Boundary Layer Ingestion Inlets With Active Flow Control. Technical Report NASA\CR-2003-212670, National Aeronautics and Space Administration, December 2003.

R.O. Dietz and M.L. Laster. Wind Tunnel Corrections for High Angle of Attack Models. Technical Report AGARD-R-692, AGARD, February 1981.

W.M. Douglass. Propulsive Efficiency with Boundary Layer Ingestion. Technical Report MDC J0860, Douglas Aircraft Company, Inc., August 1970.

M. Drela. Power Balance Method in Aerodynamic Flows. *AIAA Journal*, 47(7):1761–1771, June 2009.

M. Drela. Development of the D8 Transport Configuration. 29nd AIAA Applied Aerodynamics Conference, Honolulu, HI, June 2011.

M. Drela. D8.x Aircraft Development - Update. Aero & Astro Presentaion, October 2010. URL `http://web.mit.edu/drela/Public/N+3/tasaa.pdf`.

M. Drela. Simultaneous Optimization of the Airframe, Powerplant, and Operation of Transport Aircraft. URL `http://web.mit.edu/drela/Public/papers/RAeS/rt.pdf`. visited on 2014-04-09.

M. Drela, E. Greitzer, and A. Uranga. Subsonic Civil Transport Aircraft for 2035: An Industry-NASA-University Collaborative Enterprise. In *Proceedings of the SciTech 2015 Conference*, January 2015.

B.F.R. Ewald. Wind Tunnel Wall Corrections. Technical Report AGARDograph 336, AGARD, October 1998.

Federal Aviation Administration. CFR Final Rule. URL `http://rgl.faa.gov/Regulatory_and_Guidance_Library/rgFinalRule.nsf/0/767f48f6311bfa348625703700522b0b!OpenDocument`. visited on 2014-12-01.

A.M. Ferrar, W.F. O'Brien, W.F. Ng, R. Florea, and DJ. Arend. Active Control of Flow in Serpentine Inlets for Blended Wing-Body Aircraft. *AIAA 2009-4901*, 2009.

P.N. Freuler. Boundary Layer Ingesting Inlet Design for a Silent Aircraft. Master's thesis, Massachusetts Institute of Technology (MIT), Febuary 2005.

D.K. Hall. Personal Communication, November 2014.

L.W. Hardin, G. Tillman, and O.P. Sharma. Aircraft System Study of Boundary Layer Ingesting Propulsion. *AIAA 2012-3993*, July 2012.

A.C. Huang. Personal Communication, March 2014.

International Air Transport Association (IATA). Airlines Expect 31% Rise in Passenger Demand by 2017. Press Release No.:67, December 2013. URL `http://www.iata.org/pressroom/pr/pages/2013-12-10-01.aspx`. visited on 2014-03-11.

International Civil Aviation Organization. Committee on Aviation Environmental Protection (CAEP). URL `http://www.icao.int/environmental-protection/pages/CAEP.aspx`. visited on 2014-11-30.

R.T. Kawai, D.M. Friedman, and L. Serrano. Blended Wing Body (BWB) Boundary Layer Ingestion (BLI) Inlet Configuration and System Studies. Technical Report NASA/CR-2006-214534, National Aeronautics and Space Administration (NASA), December 2006.

H.D. Kim and J.L. Felder. Control Volume Analysis of Boundary Layer Ingesting Propulsion Systems With or Without Shock Wave Ahead of the Inlet. *AIAA 2011-222*, January 2011.

W.F. Kimzey. An analysis of the influence of some external disturbances on the aerodynamic stability of turbine engine axial flow fans and compressors. Technical Report AEDC-TD-77-80, Arnold Engineering Development Center, August 1977.

H.J.M. Kok, M. Voskuijl, and M.J.L. van Tooren. Distributed Propulsion featuring Boundary Layer Ingestion Engines for the Blended Wing Body Subsonic Transport. *AIAA 2010-3064*, April 2010.

S.W. Lee and T.J. Yoon. An Investigation of Wall-Proximity Effect Using a Typical Large-Scale Five-Hole Probe. *KSMF International Journal*, 13(3):273–285, 1999.

Lehner. Lehner motoren 3040. URL `http://www.lehner-shop.com/Inrunner/Series-30/3040::7.html`. visited on 2015-01-28.

R.H. Liebeck. Design of the Blended Wing Body Subsonic Transport. *Journal of Aircraft*, 41(1):10–25, January-February 2004.

M.J. Lighthill. On sound generated aerodynamically, Part I: General Theory. *Proceedings of the Royal Society of London*, A211:564–587, 1952.

W.K. Lord, D.G. MacMartin, and T.G. Tillman. Flow Control Opportunities in Gas Turbine Engines. *AIAA 2000-2234*, 2000.

P. Lv and A.G. Rao. Conceptual Analysis of Boundary Layer Integration towards Aircraft Propulsion Integration. *21st International Symposium on Air Breathing Engines, ISABE-2013-1436*, 2013.

F.T. Lynch. A Theoretical Investigation of the Effect of Ingesting Airframe Boundary Layer Air on Turbofan Engine Fuel Consumption. Technical Report SM-23961, Douglas Aircraft Company, Inc., May 1960.

C.M. Mehalic. Effect of Spatial Inlet Temperature and Pressure Distortion on Turbofan Engine Stability. Technical Report AIAA-88-3016, NASA-TM-100850, NASA Lewis Research Center, July 1988.

MIT, Aurora Flight Sciences, Pratt & Whitney, and NASA. Aircraft and Technology Concepts for an N+3 Subsonic Transport - Phase 2, February 2014. Year 3 Status Review Presentation.

MIT internal. Boundary Layer Ingestion Benefit of the D8 Subsonic Transport. In *Proceedings of the SciTech 2015 Conference*, January 2015.

NASA. 14'x22' Subsonic Wind Tunnel (14x22), a. URL `http://www.aeronautics.nasa.gov/atp/facilities/14x22/index.html`. visited on 2014-12-01.

NASA. NASA Awards Future Vehicle Aircraft Research Contracts, b. URL `http://www.nasa.gov/home/hqnews/2008/oct/HQ_C08-060_ARMD_contracts.html#.VHtuufldWSo`. visited on 2014-11-30.

C.L. Nickol and L.A. McCullers. Hybrid Wing Body Configuration System Studies. *AIAA 2009-931*, 2009.

S.A. Pandya. Personal Communication, January 2015.

S.A. Pandya, A. Huang, A. Espitia, and A. Uranga. Computational Assessment of the Boundary Layer Ingesting Nacelle Design of the D8 Aircraft. AIAA, 52nd Aerospace Sciences Meeting, National Harbor, Maryland, ICCFD7-4304, January 2014.

A.P. Plas. Performance of a Boundary Layer Ingesting Propulsion System. Master's thesis, Massachusetts Institute of Technology (MIT), June 2006.

A.P. Plas, M.A. Sargeant, V. Madani, D. Crichton, and E.M. Greitzer. Performance of a Boundary Layer Ingesting (BLI) Propulsion System. *AIAA 2007-450*, January 2007.

Pratt & Whitney. Classic Engines - J57 (JT3) Engine, a. URL `https://www.pw.utc.com/J57_JT3_Engine`. visited on 2014-03-12.

Pratt & Whitney. Classic Engines - JT3D (TF33) Engine, b. URL `https://www.pw.utc.com/JT3D_TF33_Engine`. visited on 2014-03-12.

Aurora Flight Sciences. Aurora Flight Sciences. URL `http://www.aurora.aero/`. visited on 2014-11-08.

J. Seddon and E.L. Goldsmith. *Intake Aerodynamics*. ISBN: 0-632-04963-4. American Institute of Aeronautics and Astronautics, Inc., Reston, Virginia, second edition, 1999.

N. Siu. Personal Communication, July 2014.

A.M.O. Smith and H.E. Roberts. The Jet Airplane Utilizing Boundary layer Air for Propulsion. *Journal of the Aeronautical Sciences*, 14(2):97–109, July 1946.

L.H. Smith. Wake Ingestion Propulsion Benefit. *Journal of Propulsion and Power*, 9(1): 74–82, Jan-Feb 1993.

T.L.B. Tamigniaux and C.O. Gordon. Effect of a Nearby Solid Surface on a Five-Hole Pressure Probe. *AIAA Journal*, 24(2):335–337, 1986.

Kapton Tape. High Temperature Masking Discs, RoHS Compliant. URL `http://www.kaptontape.com/High_Temperature_Masking_Discs.php`. visited on 2014-11-13.

A. Uranga, M. Drela, E. Greitzer, N. Titchener, M. Lieu, N. Siu, A. Huang, G. Gatlin, and J. Hannon. Preliminary Experimental Assessment of the Boundary Layer Ingestion Benefit for the D8 Aircraft. AIAA Paper, 52nd AIAA Aerospace Sciences Meeting, National Harbor, MD, January 2014.

A. Uranga, M. Drela, D.K. Hall, and E. Greitzer. Power Balance Assessment of BLI Benefits for Civil Aircraft. In *Proceedings of the SciTech 2015 Conference*, January 2015.

Appendix A

Summary of the Reported BLI Benefits in Literature

Table A.1: BLI-Benefit

Who	Metric	BLI Benefit	Note
Analytical			
Lynch (1960)	SFC	3% 0	at cruise for turbofan, 60% BLI at cruise for a turbojet, 60% BLI
Douglass (1970)	$\Delta\eta_p/\eta_p$	28.4% 15.6%	for an ideal diffuser, 100% BLI, V_e/V_0=0.75 for an airplane, 50% BLI, V_e/V_0=1.4
Smith (1993)	PSC	up to 25%	Ideal case, with form factor, H equal to 2
Kim and Felder (2011)	Φ	up to 28%	for $P_{t,1}/P_{t,\infty}$= 0.9, FPR = 1.2, electric fan, ideal case (no losses), M=0.8
Experiments			
Atinault et al. (2013)	PSC	12-16%	M=0.2, results from experiments (blunt body placed upstream of propulsor), and RANS computations, compared to no-BLI
Uranga et al. (2014)	PSC (P_E)	6%	cruise (30-40% BLI), compared to a podded configuration
Computations			
Daggett et al. (2003)	FS	5.51% 0.42% up to 42%	with AFC, including performance losses without AFC, including performance losses for whole configuration M=0.85, Alt = 10.7 km, 30%BLI, using an improved BWB 450-1U, compared to conventional airplane
Liebeck (2004)	FBPSM	27%	for an optimized BWB configuration, only taking into account system level advantages, compared to a conventional airplane (B747, A340)
Freuler (2005)	FBS	2.3% 3.3%	for 4 engines for 8 engines, 30% BLI, compared to a podded configuration, not taking into account weight

Table A.2: BLI-Benefit (continued)

Who	Metric	BLI Benefit	Note
Kawai et al. (2006)	FB	10%	with AFC for a BWB 450-1U, M=0.85, Alt = 11.9 km, compared to conventional airplane
Plas (2006)	PSC	3.8%	for 14.8% ingested drag, compared to a podded configuration
Plas et al. (2007)	η_p	up to 1.05	H=1.6, BLI=50%, Normalized jet velocity $((U_j - U_\infty)/2u_\infty)$=0.1, compared to a podded configuration
Nickol and McCullers (2009)	ΔFB	5.2% 39%	HWB (BLI) for whole HWB configuration compared to a B777
Kok et al. (2010)	FC	5%	3 BLI engines versus 3-engine strut mounted, cruise
Hardin et al. (2012)	FBB	3-5% 10%	12.4% BLI for N+3 with larger %BLI relative to a clean-inflow, pylon mounted, advanced ultra-high-bypass (UHB) baseline turbofan, for M=0.8, alt=10.7 km
Atinault et al. (2013)	PSC	12-16%	M=0.2, results from both experiments and RANS computations
Pandya et al. (2014)	PSC (P_K)	9%	at cruise, 40% BLI, compared to a podded configuration, Figure 3.4
Drela	FBS	63% 70%	for configuration D8.2, Figure 2.3 for configuration D8.6 Using TASOPT software

Abbreviations

Alt = Altitude
FB = Fuel Burn
FBB = Fuel Burn Benefit
FBPSM = Fuel Burn Per Seat Mile
FBS = Fuel Burn Saving
FPR = Fan Pressure Ratio
FS = Fuel Saving
M = Mach number
PS = Power Saving
PSC = Power Saving Constant
SFC = Specific Fuel Consumption
$\Delta\eta_p/\eta_p = (\eta_{p_i} - \eta_p)/\eta_p$, *where subscript i denotes boundary layer ingestion*
Φ = *thrust benefit parameter,* $\frac{F - F_{P_{t,1}/p_{t,\infty}=1}}{F_{P_{t,1}}/F_{P_{t,\infty}=1}} \cdot 100\%$
F is the normalized thrust coefficient, the net thrust normalized by the inlet area and the total free stream pressure at the inlet, and P_t *the total pressure*

Appendix B

Traverse System Software

The traverse system is described in Section 4.1.4. It consists of two stepper motors, controlling two bars that are connected to ball bearings that control the two arms that determine the position of the five hole probe. The two variables that determine the position of the probe are the angles of these arms, θ_1 and θ_2. The stepper motor can only move the arms in discrete steps of 0.45°, such that only a discrete number of measurement points can be reached.

A desired grid (θ_1 and θ_2 desired) is determined, the grid points that would be measured when all points could be reached. A code was then written to determine the nearest possible point, taking into account the discrete stepsize of the stepper motors. The code first maps all the possible points, after which a least square principle is used to determine the closest possible point.

B.1 Coordinate System Definition

Figure B.1 gives the coordinate system definitions for the traverse system. The traverser center (red dot in Figure B.1, 'Trav center') is the zero point, from which the position of the measurement point (tip of the probe) is referenced by Equations B.1 and B.2.

$$y = +\text{arm}_1 \cdot cos(\theta_1) + \text{arm}_2 \cdot cos(\theta_2) \tag{B.1}$$

$$z = -\text{arm}_1 \cdot sin(\theta_1) - \text{arm}_2 \cdot sin(\theta_2) \tag{B.2}$$

where y and z are the coordinates displayed in Figure B.1. Arm$_1$ and arm$_1$ are the lengths of the arms and θ_1 and θ_2 are the angles of the arms, defined in Figure B.1.

A reference point is chosen to link the coordinate system of the D8 wind tunnel model to the coordinate system of the traverse system. This reference point is displayed in Figure B.1 by a red dot ('Ref'), and is located on top of the screw that attaches the mini beaver tail to the model. Several length definitions are used in Figure B.1:

- YpropAbs = 96.0 mm
- ZprobAbs = 203.2 mm
- YtravAbs = 0 mm
- ZtravAbs = 13.2 mm
- arm_1=123.9 mm
- arm_2=169.4 mm

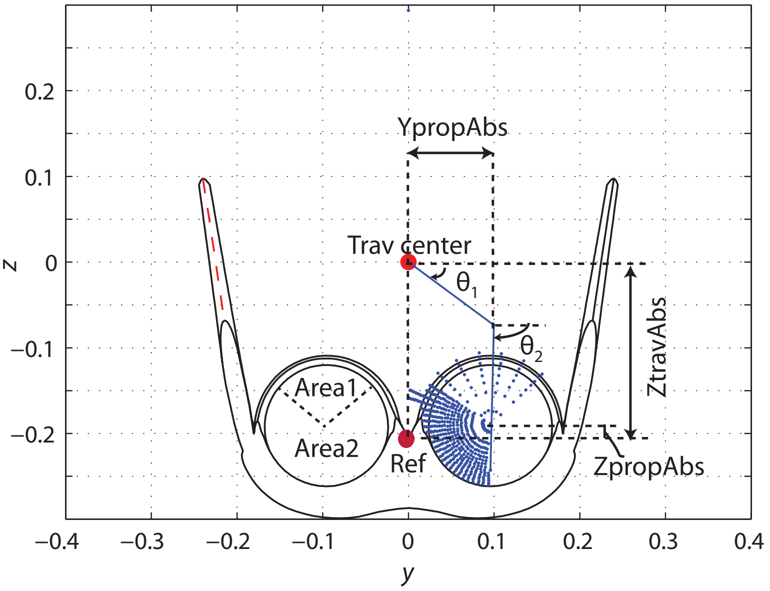

Figure B.1: Integrated inlet conventions

B.2 MATLAB Code Set-up

One MATLAB code is written to generate the grids for the integrated exit, integrated inlet, and podded exit. In this thesis only the integrated inlet is considered, however, the general code set-up is explained.

The MATLAB code consists of a main script *GetThetas.m*, two functions to generate the inlet and exit grid, *Generate_inlet_grid.m* and *exitflow_genGrid_airframe.m*, a function to calculate the closest possible point, *MatchTheta.m*, *.mat*-files with the model coordinates, *.dat*-files with the coordinates of the bifurcation, and input *.m*-files for the main script for each configuration with the specific variables for each configuration, such as the dimensions. The function *exitflow_genGrid_airframe.m* was written by Siu (2014), who performed previous measurements at the exit of the propulsor.

In the main script the configuration is specified, after which the input file for that configuration is loaded to get the dimensions needed. The grid is then generated using the function *Generate_inlet_grid.m* or *exitflow_genGrid_airframe.m*. This is the desired grid (red dots in Figure B.2). The function *MatchTheta.m* calculates all points that can be reached taking into account the stepsize of 0.45°and uses a least square principle to determine which of the possible points is closed to the desired point. The output of the function *MatchTheta.m* are θ_1 and θ_2, corresponding to Y and Z values of the actual grid (blue dots in Figure B.2).

The main script then adds an move in, move out and in some cases a move left-right maneuver to the ouput of the function *MatchTheta.m*. The move in maneuver is the maneuver to move the probe from the initial position to the first grid point, the move out maneuver is the maneuver to move from the last grid point position back to the initial position and the move left-right maneuver is the maneuver to move from one propulsor to the other propulsor.

The final output of *GetThetas.m* is a *.txt*-file with a list of θ_1 and θ_2 that can be loaded into LABview to control the stepper motors.

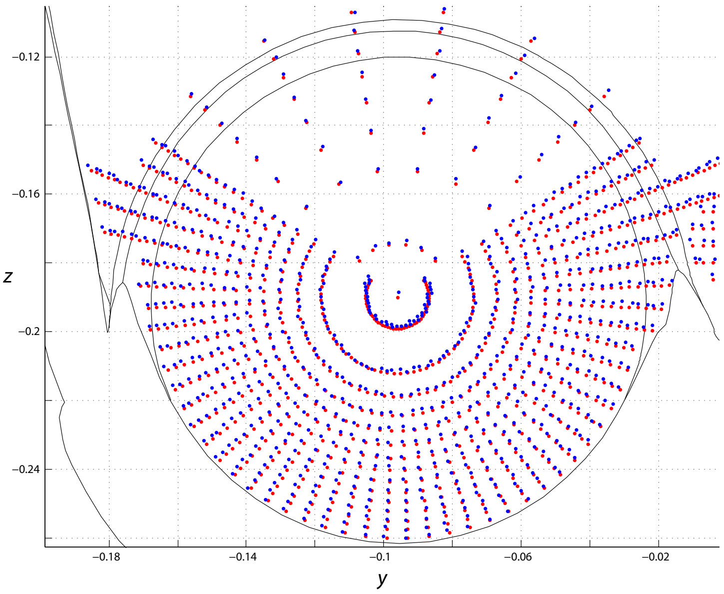

Figure B.2: Desired (red) and actual (blue) grid for the integrated inlet configuration

The values of theta are sorted in such a way that the traverser path follows the spokes from outside to inside and then from inside to outside. This is the fastest way of traversing. The complete traverser path is illustrated in Figure B.3.

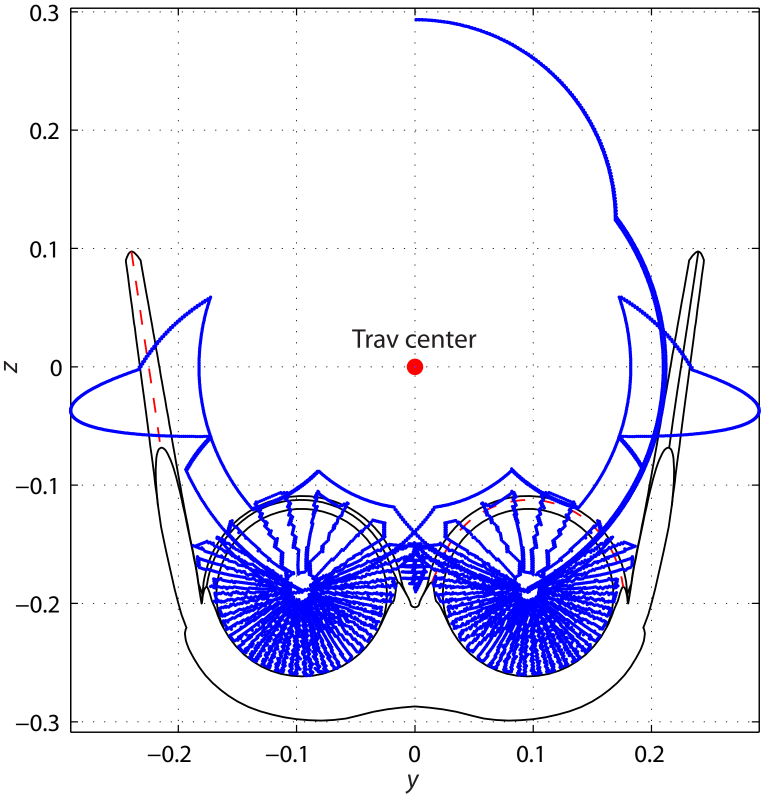

Figure B.3: Taverser path, integrated inlet (fine)

Appendix C

Streamlines CFD

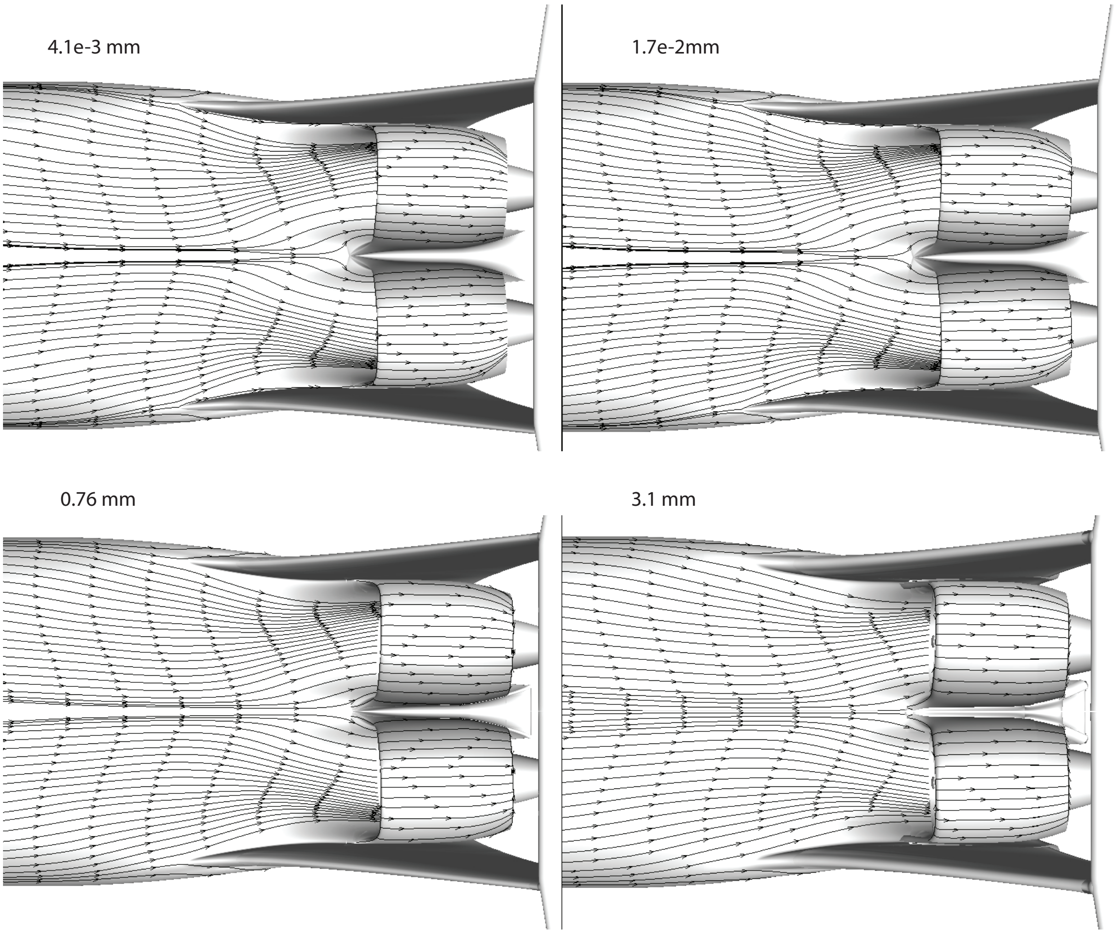

Figure C.1: Streamlines CFD, $4.1{\cdot}10^{-3}$, $1.7{\cdot}10^{-3}$, 0.76 and 3.1 mm above the surface, cruise condition

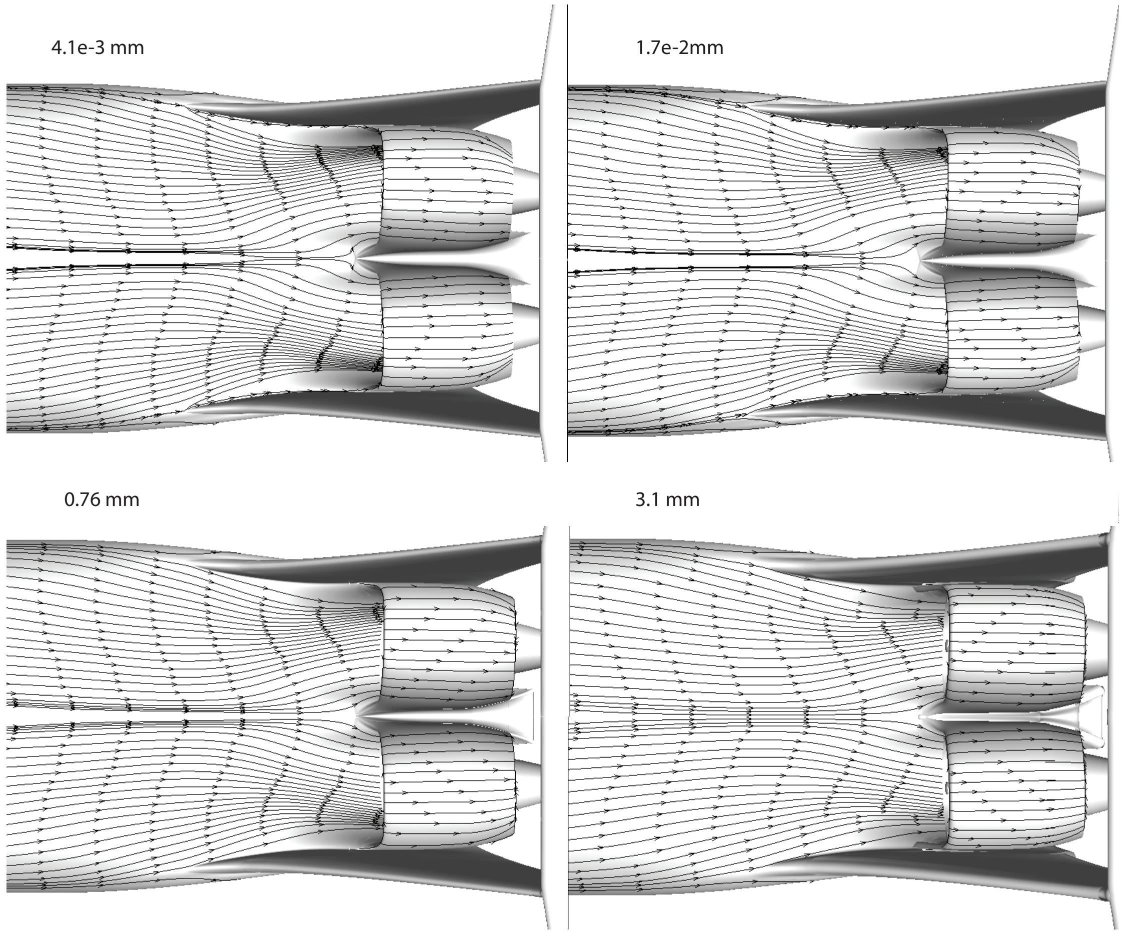

4.1e-3 mm

1.7e-2mm

0.76 mm

3.1 mm

Figure C.2: Streamlines CFD, $4.1 \cdot 10^{-3}$, $1.7 \cdot 10^{-3}$, 0.76 and 3.1 mm above the surface, top of climb condition

Appendix D

Effect of Angle of Attack - Mini-Tufts

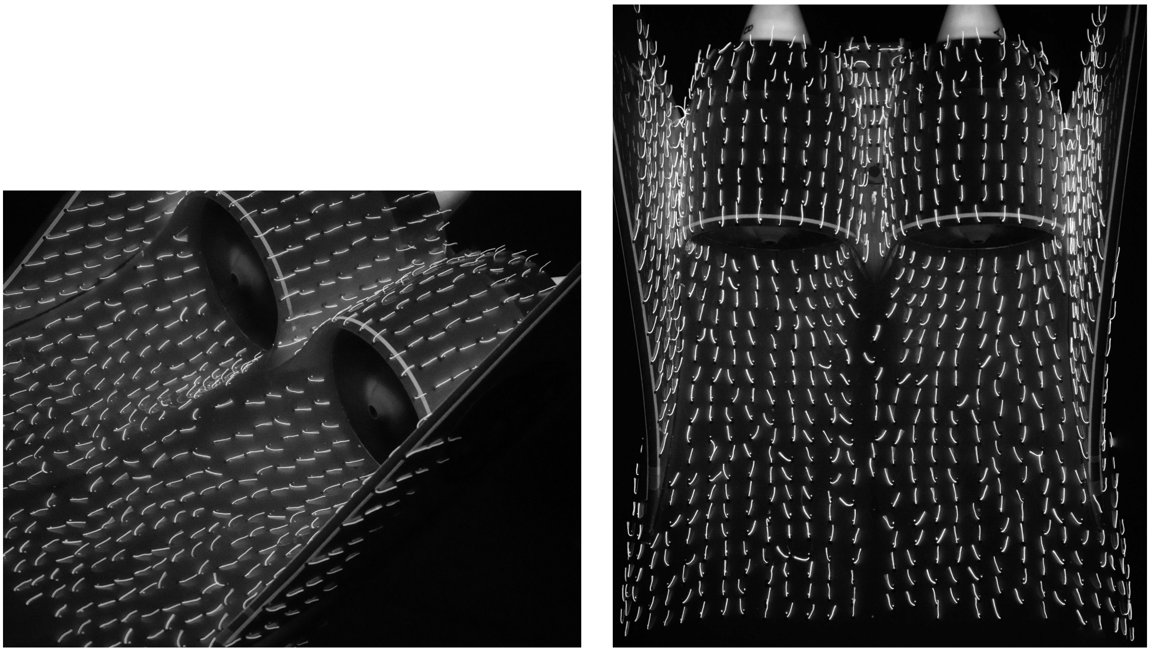

Figure D.1: Results mini-tufts flow visualization, α=2°, λ=3.4

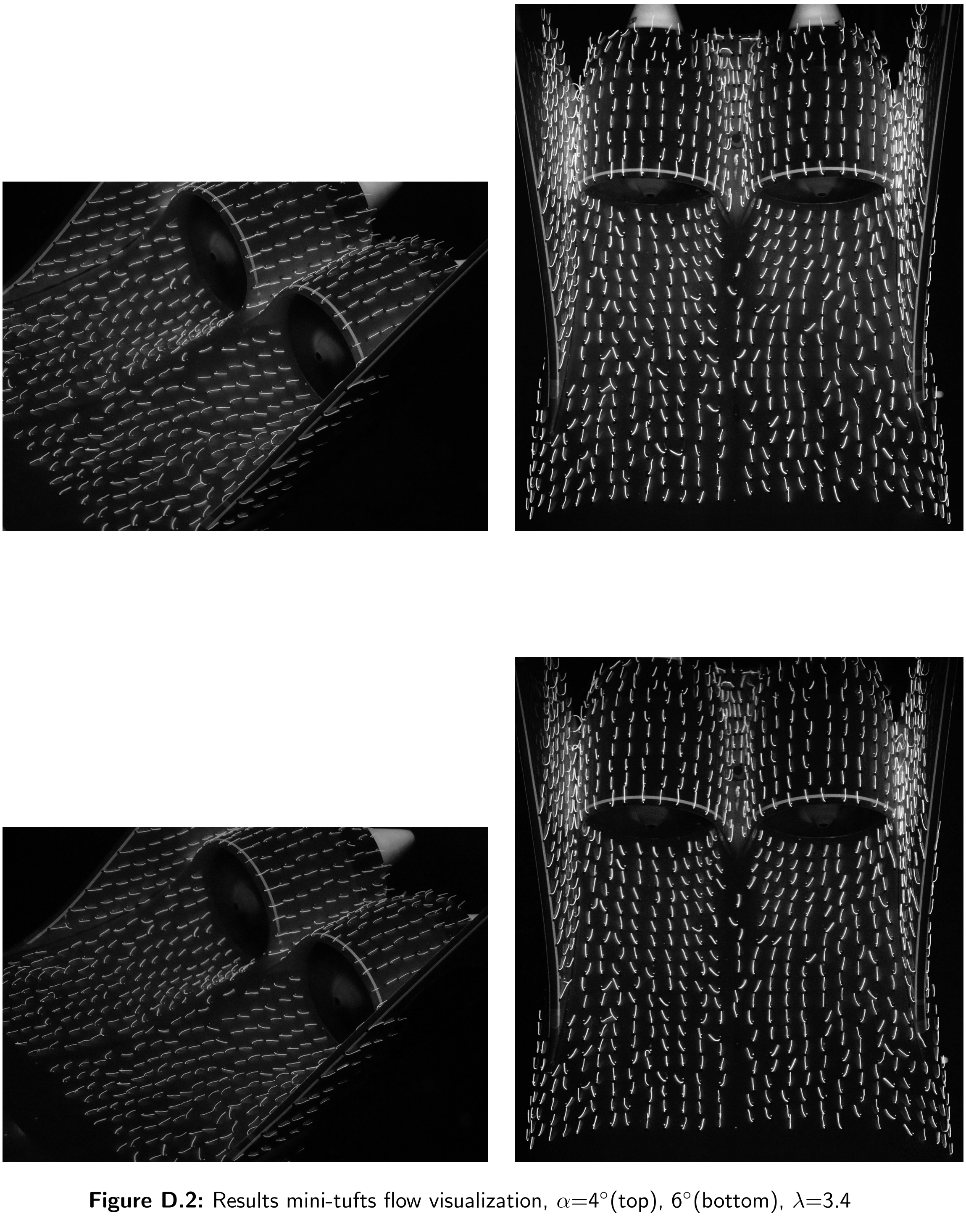

Figure D.2: Results mini-tufts flow visualization, α=4°(top), 6°(bottom), λ=3.4

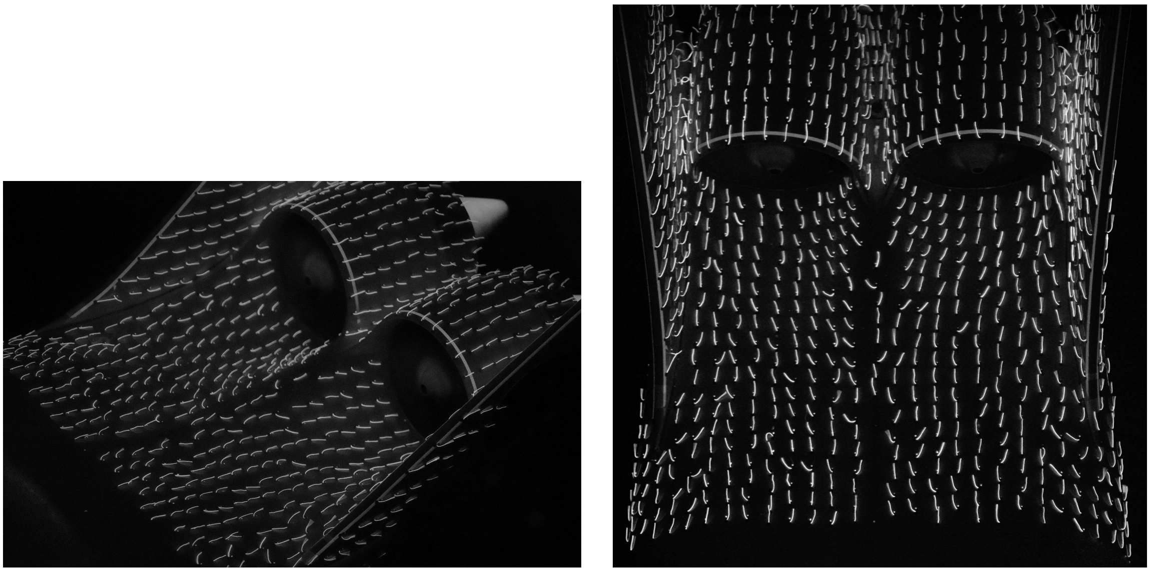

Figure D.3: Results mini-tufts flow visualization, α=8°, λ=3.4